

UNCLASSIFIED

AD 400 700

*Reproduced
by the*

**ARMED SERVICES TECHNICAL INFORMATION AGENCY
ARLINGTON HALL STATION
ARLINGTON 12, VIRGINIA**



UNCLASSIFIED

NOTICE: When government or other drawings, specifications or other data are used for any purpose other than in connection with a definitely related government procurement operation, the U. S. Government thereby incurs no responsibility, nor any obligation whatsoever; and the fact that the Government may have formulated, furnished, or in any way supplied the said drawings, specifications, or other data is not to be regarded by implication or otherwise as in any manner licensing the holder or any other person or corporation, or conveying any rights or permission to manufacture, use or sell any patented invention that may in any way be related thereto.

62-3-1

400 700

6130-6259-KU-000

BSD-TDR-62-354

CATALOGED BY ASTIA
AS AD NO. 200700

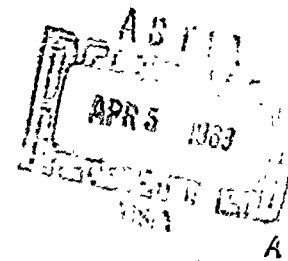
EFFECT OF NOSE BLUNTNESS ON THE TURBULENT HYPERSONIC WAKE

By Leslie Hromas
and Lester Lees

OCTOBER 1962

Contract No. AF 04(694)-1

Prepared for
HQ BALLISTIC SYSTEMS DIVISION
AIR FORCE SYSTEMS COMMAND
UNITED STATES AIR FORCE
Air Force Unit Post Office, Los Angeles 45, California
Attention TDC



SPACE TECHNOLOGY LABORATORIES, INC
a subsidiary of Thompson Ramo Wooldridge Inc.
ONE SPACE PARK • REDONDO BEACH, CALIFORNIA

BSD-TDR-62-354

EFFECT OF NOSE BLUNTNESS ON THE
TURBULENT HYPERSONIC WAKE

Prepared by

Leslie Hromas

and

Lester Lees

SPACE TECHNOLOGY LABORATORIES, INC.

Los Angeles 45, California

6130-6259-KU-000

Contract No. AF 04(694)-1

October, 1962

Prepared for

HQ BALLISTIC SYSTEMS DIVISION
AIR FORCE SYSTEMS COMMAND
UNITED STATES AIR FORCE
Air Force Unit Post Office, Los Angeles 45, California
Attention: TDC

Prepared for
HQ BALLISTIC SYSTEMS DIVISION
AIR FORCE SYSTEMS COMMAND, USAF
Under Contract AF 04(694)-1

Prepared by: Leslie A. Hromas
Leslie A. Hromas
Aerosciences Laboratory
Research Staff

Prepared by: Lester Lees
Lester Lees
Consultant and Professor
of Aeronautics, California
Institute of Technology

Approved by: A. G. Hammitt
A. G. Hammitt, Manager
Aerosciences Laboratory
Research Staff

SPACE TECHNOLOGY LABORATORIES, INC.
A Subsidiary of Thompson Ramo Wooldridge, Inc.
One Space Park • Redondo Beach, California

ABSTRACT

The effect of body geometry on the equilibrium turbulent hypersonic wake is examined by computing the wakes behind several bodies with different cone and sphere-cone nose shapes. Typical re-entry trajectories at several different altitudes are used for the free stream conditions. Also, theoretical predictions for the wake growth behind cones are compared with available ballistic range measurements.

In order to determine the initial conditions for the subsequent wake behavior the bow shock shape, the viscous base and neck regions, and the inviscid wake shock are examined. The results for the initial wake properties indicate that the inviscid flow is made cold by making the body sufficiently slender, even though the wake shock now gives a relatively significant contribution to the enthalpy. Also it is found that in determining the initial viscous core properties the Reynolds number is much more important than the shape of the body.

From the downstream wake histories the results indicate that initially the slender body wake grows slower and cools much faster than the blunt body wake. Eventually, sufficiently far downstream the wakes of all bodies should be a unique function of $C_D A$. However, until the asymptotic downstream conditions occur, it is found that even two bodies with the same drag coefficient but different shapes can have completely different wake growth and enthalpy histories. Further, the degree of this difference depends considerably on the altitude (Reynolds number). Since equilibrium electron histories follow the enthalpy, a slender cone can have a very short radar wake compared to a blunt body. On the other hand, because of the initially slower wake growth for the cone an even longer time than for the blunt body can be required for the radial diffusion of any non-recombining foreign substance (e.g., ablation material) deposited in the wake.

CONTENTS

List of Figures

List of Symbols

1. Introduction
2. Summary of Theory
 - 2.1. Turbulent Diffusion of Enthalpy in the Inner Wake
 - 2.2. Turbulent Mass Diffusion in the Inner Wake
3. Bow Shock Shape
4. Base and Neck Properties
 - 4.1. Free Shear Layer
 - 4.1.1. Velocity Along Dividing Streamline
 - 4.1.2. Inviscid Free Streamline
 - 4.2. Initial Viscous Core Properties
 - 4.2.1. Initial Core Drag $(C_{D_f})_1$
 - 4.2.2. Turbulent Front Location
 - 4.2.3. Initial Level of Enthalpy on Axis
 - 4.3. Wake Shock
5. Pressure Distribution, Pressure Drag and Initial Wake Enthalpy Distributions
 - 5.1. Pressure Distribution
 - 5.2. Inviscid Forebody Drag Coefficient (Pressure Drag)
 - 5.3. Initial Wake Inviscid Enthalpy Distribution
6. Discussion of Downstream Wake Properties
 - 6.1. Wake Growth
 - 6.1.1. Effect of Shape Variation (Blunt vs. Sharp)
 - 6.1.2. Effect of Shape Variation (Same Drag Coefficients)
 - 6.1.3. Effect of Altitude Variation

CONTENTS (Cont'd.)

- 6.2. Enthalpy and Velocity Distributions
- 6.3. Electron Decay
 - 6.3.1. Equilibrium Flow Conditions
 - 6.3.2. Pure Mass Diffusion
- 6.4. Effect of Accuracy of Initial Wake Conditions
- 7. Conclusions
- References

LIST OF FIGURES

1. Wake Behind Blunt Body at Hypersonic Speeds
2. Body Geometry Schematic
3. Inviscid Flow Configuration for Slender Body
4. Bow Shock Wave Characteristics for Various Sphere-Cone Combinations ($M_\infty = 22$, $ht = 100,000$ ft., $\theta_c = 120^\circ$)
5. Computed and Experimental Shock Shapes for Various Sphere-Cones Including Wake Shock
6. Computed Bow Shock Shapes for Various Cones ($M_\infty = 22$, $ht = 100,000$ ft.)
7. Computed Bow and Wake Shock Shapes for Slender Cones ($M_\infty = 5.9, 7.8$, and 22)
8. Comparison of Theoretical and Experimental Shock Shape ($R_{N/R_B} = 1/2$)
9. Variation of n_2 , $Y_{L_{se}}$ and $(Y_{L_{f1}})$ vs. Cone Angle
10. Variation of n_2 and $Y_{L_{se}}$ vs. Drag Coefficient
11. Correlated Bow Shock Shapes for Various Sphere-Cone Combinations
12. Mixing Layer Velocity as a Function of Mass Flow Parameter for Different Lengths of Separated Mixing Layer
13. Incompressible and Compressible Boundary Layer Profiles Before and After Base Region Expansion
14. Axis-Symmetric Effect on Base Region Free Streamline ($M_\infty = 22$, $ht = 100,000$ ft., $\theta_c = 120^\circ$)
15. Drag Contributions Due to Pressure and Skin Friction for a Cone ($M_\infty = 22$, $ht = 100,000$ ft.)
16. Surface and Wake Pressure Distributions for Various Sphere-Cone Combinations
17. Surface and Wake Pressure Distributions for Various Cones ($M_\infty = 22$, $ht = 100,000$ ft.)

LIST OF FIGURES (Cont'd.)

18. Surface and Wake Pressure Distribution for Ballistic Range Data
19. Drag Coefficient for Sphere-Cones (Hypersonic)
20. Effect of Wake Shock on Enthalpy Distribution for Conical Body ($M_\infty = 5.9$, $p_\infty = .071$)
21. Effect of Wake Shock on Enthalpy Distribution for Conical Body ($M_\infty = 22$, $ht = 100,000$ ft.)
22. Inviscid Enthalpy Profiles ($M_\infty = 22$, $ht = 100,000$ ft.)
23. Comparison of Theory and Experiment on Turbulent Wake Width ($M_\infty = 5.9$, $\theta_c = 12.5^\circ$)
24. Comparison of Theory and Experiment on Turbulent Wake Width ($M_\infty = 7.8$, $\theta_c = 25^\circ$)
25. Comparison of Turbulent Wake Width for Different Nose Bluntness ($M_\infty = 22$, $ht = 100,000$ ft.)
26. Effect of Nose Bluntness on Growth of Turbulent Wake, "Reduced" Coordinates ($M_\infty = 22$, $ht = 100,000$ ft.)
27. Growth of Turbulent Wake for a Blunt Nosed and a Sharp Nosed Body With the Same C_{DA}
28. Growth of Turbulent Wake for a 12° Cone at Various Altitudes ($M_\infty = 22$)
29. Equilibrium Enthalpy and Velocity Distributions Along Wake Axis and Turbulent Front ($M_\infty = 22$, $ht = 100,000$ ft.)
30. Equilibrium Enthalpy and Velocity Distributions Along Wake Axis for a Blunt Nosed and a Sharp Nosed Body with the same C_{DA} ($M_\infty = 22$, $ht = 100,000$ and $150,000$ ft.)
31. Effect of Nose Bluntness on Electron Density Along Wake Axis ($M_\infty = 22$, $ht = 100,000$ ft.)
32. Wake Length as a Function of Drag Coefficient ($M_\infty = 22$, $ht = 100,000$ ft., $\theta_c = 12^\circ$)

LIST OF SYMBOLS

A	area
$B_1 \left(\frac{x-x_1}{d} \right)$	enthalpy function defined in Eq. (5)
C	Chapman viscosity constant
C_D	total drag coefficient defined in Eq. (9).
C_{D_o}	outer inviscid flow drag coefficient based on free stream quantities
C_{D_f}	turbulent inner wake drag coefficient based on free stream quantities
ΔC_{D_f}	drag coefficient associated with wake shock
d	body diameter
D	drag
$F \left(\frac{Y_T}{Y_{T_D}} \right)$	mass fraction function defined in Eq. (13)
$F_1(Y_{L_f})$	drag function defined in Eq. (8)
$F_2(Y_{L_f})$	function defined in Eq. (12d)
$g(Y_L)$	enthalpy function defined in Eq. (2)
$G \left(\frac{Y_T}{Y_{T_f}} \right)$	enthalpy function defined in Eq. (5)
$G_m + 1$	function defined in Eq. (5a)
h	static enthalpy
H	enthalpy ratio, $\left(\frac{h_L}{h_\infty} - 1 \right)_o$
\bar{H}	stagnation enthalpy
k	shock wave constant defined in Eq. (16)
K"	skin friction constant defined in Eq. (19)

LIST OF SYMBOLS (Cont'd.)

K'	diffusivity function defined in Eq. (7)
K	diffusivity constant, $K' \left(\frac{\rho(o)}{p_f} \right)^{\frac{1}{m+1}}$
K_o	axial mass fraction defined in Eq. (13)
l	length of mixing run
l_o	Townsend's wake width
M	Mach number
n_e	electron $/cm^3$
n_I	particle number density
n_1	bow shock exponent defined on Page 9
n_2	bow shock exponent defined on Page 9
n_w	wake shock exponent defined on Page 9
p	pressure
R_B	body base radius
R_N	body nose radius
Re	Reynolds number
R_T	Townsend's "universal" Reynolds number $\frac{l_o(u_f - u(0))}{\epsilon_T}$
u	axial velocity component
u^*	velocity along base region dividing streamline
x	axial coordinate
y	radial coordinate

LIST OF SYMBOLS (Cont'd.)

\tilde{y}	$\frac{y}{d}$
Y	Howarth-Dorodnitsyn coordinate
β	velocity ratio, $\frac{u}{u_{\infty}}$
γ	ratio of specific heats
δ	mass constant defined in Eq. (10); also boundary layer thickness
ϵ_T	turbulent thermal diffusivity
ζ	Chapman mass parameter defined on Page 12
θ	angle
χ_i	mass fraction
ξ	mixing parameter defined in Eq. (17)
ρ	density
ψ	stream function

LIST OF SYMBOLS (Cont'd.)

SUBSCRIPTS

c	cone
e	intersection of shoulder Mach wave and bow shock, also free streamline
f	front
i	initial; also species and incompressible
L	outer inviscid
0	along axis
s	shock
T	turbulent
w	wall
1	shoulder
2	expansion region
3	behind wake shock
∞	free stream

1. INTRODUCTION

The turbulent wake behind a body moving at hypersonic speeds can be considered to be composed of two portions (Fig. 1); an outer inviscid region and an inner turbulent viscous core. For a blunt body the large nearly-normal portion of the bow shock generates very high flow temperatures, with the result that under equilibrium conditions the outer inviscid region remains hot even after isentropic expansion to ambient pressure. Furthermore the turbulent core itself, which has undergone viscous losses around the body and in the free shear layer, can also be hot. The subsequent cooling process by core growth and turbulent mixing, although much faster than laminar diffusion, has been found (1)⁺ to require distances of hundreds of body diameters downstream, largely because the hot core is surrounded and fed by additional hot gas from the outer inviscid region. The purpose of this paper is to examine the effect of body geometry on the turbulent wake. This will be accomplished by computing the wakes for bodies of various bluntness ratios (nose/base diameter) and comparing with the previously computed sphere (1).

It is necessary to examine the changes produced by body shape in both the outer inviscid flow and the initial turbulent core or neck properties. Since the bow shock strength is nearly everywhere quite weak, the inviscid flow changes considerably and, in fact, should be made "cold" by making the body slender. The contribution of the wake shock for a blunt body was found to be negligible (1) in comparison with the bow shock, and now must be re-examined for a slender body.

Regarding the viscous core properties it is not possible to state a priori what is the effect of changing body shape. Conventional methods of calculating the boundary and free shear layers were used; however, clearly more detailed analysis of the latter and, above all, experimental data at the higher velocities are needed. For example, the basic structure of the wake neck geometry at high velocities ($M_\infty \approx 20$) would be very useful.

Two important physical processes determining the properties of the turbulent wake are non-equilibrium chemical processes and body ablation characteristics. Discussion and preliminary results regarding the former as to hypersonic wake flows are given by Lees (2) and Bloom (3). For the present,

⁺ Denotes references listed at end of paper.

we assume here chemical equilibrium of pure air, except that the special case of "pure" diffusion of a foreign species with zero recombination is considered.

Two families of bodies are considered here. These are shown in Fig. 2 with the pertinent flow properties given in Tables I and II. One of these families consists of sphere-cones with a constant cone angle. The second family are pure cones of various angles. The wakes are calculated for typical re-entry conditions of $M_\infty = 20.32$ (Table I) at various altitudes (Reynolds number variations). Also, theoretical predictions for the wake growth behind cones are compared with ballistic range data taken by Slattery (4) and Gray and Siperly (5) and Short (Table II).

In Section 2, a brief resume of the theoretical relations is included in order to provide a convenient reference. For shock shapes for the various bodies are examined in Section 3. In Section 4 the methods used to calculate the case and neck properties are described while in Section 5 the complete initial inviscid wake enthalpy distributions are given. Discussion of the downstream turbulent wake properties is given in Section 6 and conclusions from this study in Section 7.

2. SUMMARY OF THEORETICAL ANALYSIS

2.1. Turbulent Diffusion of Enthalpy in the Inner Wake

Since the details of the analysis used here have been published in Ref. (1), only essential points and relations are listed below.

1. Howarth-Dorodnitsyn variable is used for the inviscid regime

$$Y_L^m dY_L = \left(\frac{\rho_L}{\rho_\infty} \right) \tilde{y}^m d\tilde{y} \quad (1)$$

where $\tilde{y} = y/\bar{a}$ and the subscript L denotes inviscid or outer wake properties.

2. Inviscid enthalpy is characterized by a two parameter relation

$$\frac{h_L}{h_\infty} - 1 = \left[\frac{h_L}{h_\infty} - 1 \right]_0 g(Y_L) = Hg(Y_L) \quad (2)$$

⁺ $m = 0$ for two dimensional flow and $m = 1$ for axi-symmetric flow.

3. Velocity is assumed to be an average velocity ($u = \beta u_\infty$) where $0.8 < \beta < 0.9$ so

$$\frac{u_\infty - u}{u_\infty} \ll 1 \text{ and } h - h_\infty \approx \beta u_\infty (u_\infty - u) \quad (3)$$

4. Howarth-Dorodnitsyn variable for the turbulent core is referenced to the front values at $\tilde{y} = \tilde{y}_f$

$$Y_T^m d Y_T = \left(\frac{\rho}{\rho_f} \right) \tilde{y}^m d \tilde{y} \quad (4)$$

5. Profile within the turbulent core is characterized by two parameters

$$\frac{h_T - h_f}{h_\infty} = B_1 \left(\frac{x - x_1}{d} \right) G \left(\frac{Y_T}{Y_{Tf}} \right) \quad (5)$$

where for the present $G \left(\frac{Y_T}{Y_{Tf}} \right)$ is assumed parabolic and the following will be used

$$G_{m+1} = \int_0^1 G \left(\frac{Y_T}{Y_{Tf}} \right) \left(\frac{Y_T}{Y_{Tf}} \right)^m d \left(\frac{Y_T}{Y_{Tf}} \right) \quad (5a)$$

6. Reynolds' hypothesis of similarity between the turbulent transfer of mass, momentum and energy is assumed. Thus only the thermal diffusivity is needed. Townsend (1) found that for low speed wakes

$$R_T = \frac{[u_f - u(0)] \ell_0}{\epsilon_T} = \text{constant} \quad (6)$$

where ℓ_0 is a measure of the wake width. The assumption is now made that the hypersonic wake instantaneously acts like a slice of low speed wake or

$$\epsilon_T = K' [u_f - u(0)] y_f \quad (7)$$

where K' can be related to Townsend's R_T by $K' = \left(\frac{\rho(0)}{\rho_f} \right)^{\frac{1}{m+1}} \frac{1}{R_T}$

7. Only the thermodynamic effect of the static pressure variations along the wake axis is considered, i.e., the pressure gradient terms in the governing equations are neglected but the equation of state p/ρ is used. By integrating the energy equation across the wake results in the following relation between the two parameters $B_1 \left(\frac{x}{d} \right)$ and $Y_{T_f} \left(\frac{x}{d} \right)$

$$\left[\left(\frac{\rho_f}{\rho_\infty} \right) B_1 Y_{T_f}^{m+1} G_{m+1} \right]_i = \left(\frac{C_{D_f}}{C_{D_i}} \right)_i = F_1 \left(\frac{x}{L_c} \right) = 1 + \frac{H}{H+1} \left[3 \left(\frac{Y_{L_f}}{Y_{L_i}} \right) - 2 \left(\frac{Y_{L_f}}{Y_{L_i}} \right)^2 \right] + \frac{4}{(\gamma-1) M_\infty^2 (C_{D_i})_i} \left\{ \int_{Y_{L_f,i}}^{Y_{L_f}} \varepsilon \left(\frac{Y_{L_f}}{Y_{L_i}} \right) Y_{L_f}^m d Y_{L_f} - \left[\frac{\varepsilon \left(\frac{Y_{L_f}}{Y_{L_i}} \right) Y_{L_f}^{m+1}}{H+1} \right]_{Y_{L_f,i}}^{Y_{L_f}} \right\} \quad (8)$$

Note that this relation gives the comparison of instantaneous core drag to initial drag. Thus asymptotically far down stream

$$C_{D_o} + C_{D_f} = C_D = \left[\left(\frac{C_{D_f}}{C_{D_i}} \right)_i F_1 \left(\frac{Y_{L_f}}{Y_{L_i}} \right) \right]_{\frac{x}{d} \rightarrow \infty} \quad (9)$$

Also in Eq. 8 the fact is used that the turbulent and inviscid Howarth coordinates (Y_{T_f}, Y_{L_f}) are related by

$$\frac{\rho_f}{\rho_\infty} Y_{T_f}^{m+1} = Y_{L_f}^{m+1} - \delta (\text{constant}) \quad (10)$$

where

$$\delta = \frac{(m+1)(\gamma-1)M_\infty^2}{(H+1)4^{m+1}} C_{D_{f,i}}$$

8. A second relation between $B_1 \left(\frac{x}{d} \right)$ and $Y_{T_f} \left(\frac{x}{d} \right)$ is obtained by satisfying the energy equation along the axis. Finally, using this relation and Eqs. (1 - 10) leads to an integral equation for the wake growth Y_{L_f} :

$$\int_{Y_{L_f 1}}^{Y_{L_f}} \left[\frac{Y_{L_f}^{m-1} (Y_{L_f}^{m+1} - \delta)^{\frac{2}{m+1}} \left(\frac{h(0)}{h_\infty} \right)^{\frac{1}{m+1}} \left(\frac{h_f}{h_\infty} \right)^{\frac{1}{m+1}}}{\left[\left(\frac{p(c)}{p_\infty} \right)^{\frac{1}{m+1}} \frac{\tilde{y}_f}{Y_{L_f}} \right]} \cdot \frac{F_2(Y_{L_f})}{F_1(Y_{L_f})} \right] d Y_{L_f} +$$

$$= - \frac{K}{\beta^2} \cdot \frac{g''(0)}{4^{m+1} G_{m+1}} \left(C_{D_f} \right)_1 \int_{\frac{x}{d}}^{\frac{x}{d}} \left(\frac{p(0)}{p_\infty} \right)^{\frac{1}{m+1}} d \left(\frac{x}{d} \right) \quad (11)$$

where

$$\frac{h_f}{h_\infty} = 1 + Hg(Y_{L_f}) \quad (12a)$$

$$\frac{h(0)}{h_\infty} = 1 + H \left[g(Y_{L_f}) + \underbrace{\frac{(\gamma-1) M_\infty^2 (C_{D_f})_1 F_2(Y_{L_f})}{4^{m+1} G_{m+1} H(Y_{L_f}^{m+1} - \delta)}}_{\frac{B_1}{H}} \right] \quad (12b)$$

$$\left(\frac{p(0)}{p_\infty} \right)^{\frac{1}{m+1}} \frac{\tilde{y}_f}{Y_{L_f}} = \left[1 + \frac{(m+1)H}{Y_{L_f}^{m+1}} \int_0^{Y_{L_f}} Y_{L_f} g(Y_{L_f}) d Y_{L_f} \right]^{\frac{1}{m+1}} \quad (12c)$$

$$F_2(Y_{L_f}) = \left[1 + \frac{1}{m+1} \left\{ \frac{1}{(m+1)G_{m+1}} - 1 \right\} \frac{Hg'(Y_{L_f})(Y_{L_f}^{m+1} - \delta)^{\frac{2}{m+1}} 4^{m+1} G_{m+1}}{(\gamma-1) M_\infty^2 (C_{D_f})_1 Y_{L_f}^m F_1(Y_{L_f})} \right] \quad (12d)$$

* Prime denotes differentiation.

2.2 Turbulent Mass Diffusion in the Inner Wake

Once the history of the turbulent diffusivity $\epsilon_T(\frac{x}{d})$ along the wake axis is known, turbulent diffusion of a particular species in the inner wake can be described by an analysis similar to that for the enthalpy. It is assumed the mass concentration is again given by a two parameter relation

$$\chi_i(\frac{x}{d}, Y_T) = K_0(\frac{x}{d}) F\left\{\frac{Y_T}{Y_{TD}(\frac{x}{d})}\right\} \quad (13)$$

where F is taken to be gaussian. The result as given in Ref. (1) for the variation of $K_0(\frac{x}{d})$ along the axis is

$$\left[\frac{K_0(\frac{x}{d})_1}{K_0(\frac{x}{d})}\right]^{\frac{2}{m+1}} = 1 + \frac{2 K(C_{Df1})}{4^m G_{m+1} \beta^2 (Y_{Lf} - \delta)^{2/m+1}} \int_{\frac{x}{d}_1}^{\frac{x}{d}} \frac{\left(\frac{p_f}{p_\infty}\right)^{\frac{2}{m+1}} \tilde{y}_f \cdot F_1\left(\frac{Y_{Lf}}{Y_{Lf} - \delta}\right)}{\left(\frac{h_f}{h_\infty}\right)^{\frac{1}{m+1}} \left(\frac{h(0)}{h_\infty}\right)^{\frac{1}{m+1}} \left(\frac{Y_{Lf}}{Y_{Lf} - \delta}\right)^{m+1}} d\left(\frac{x}{d}\right) \quad (14)$$

Once the mass fraction is known the value of the number density per unit volume along the axis is calculated from the relation

$$\frac{n_1\left(\frac{x}{d}, 0\right)}{n_r\left(\frac{x}{d}, 0\right)} = \frac{\left(\frac{p_f}{p_\infty}\right)\left(\frac{h(0)}{h_\infty}\right)_1}{\left(\frac{p_f}{p_\infty}\right)_1 \left(\frac{h(0)}{h_\infty}\right)} \cdot \frac{K_0\left(\frac{x}{d}\right)}{K_0\left(\frac{x}{d}\right)_1} \quad (15)$$

The relations as given above are in a slightly different form from those in Ref. (1). This is because the over-all inviscid drag coefficient C_{D^0} was introduced as a normalizing factor in the former. It is not necessary to do this since the behavior of the core depends only on the location of the local enthalpy front and its slope; it knows nothing of the over-all drag until it has engulfed the complete inviscid drag.

3. BOW SHOCK SHAPE

The turbulent wake analysis assumes that the outer inviscid enthalpy profile is invariant with axial distance, which will be the case once the pressure returns to ambient. Since the entropy is constant along any streamline in the inviscid flow, only the shock shapes, including the wake shock, are needed to determine the desired enthalpy at $p = p_\infty$.

The general configuration of the inviscid flow field as calculated is shown in Fig. 3 where A is a constant pressure free streamline and B is a cylindrical sting. To determine the wake shock actually calls for knowledge of the viscous base and neck region, since these determine its position and the amount of recompression necessary for the flow to be turned back parallel with the axis (angle of A and position of B in Fig. 3). Strictly speaking the bow shock is also affected by the base region through the shoulder expansion fan. However, the back portion of the expansion fan, which is sensitive to the shoulder expansion angle, hits the bow shock far downstream where the shock is already quite weak. Thus an error in the estimate of the shoulder expansion angle of several degrees was found to make negligible differences in the downstream bow shock shape, and the bow shock can be studied separately without knowing exact details of the base region. The latter will be examined before the second shock and complete initial wake inviscid enthalpy profiles are given.

For each of the configurations studied these shock shapes were obtained by the method of characteristics⁺. Emphasis is placed here on the use of the shock shape rather than the detailed characteristics solution throughout the flow field since extension of characteristics calculations well downstream is apt to introduce significant errors, especially in high entropy gradient flows (1, 6). The details of the body shapes and flow parameters are found in Fig. 2 and Tables I and II.

Blast wave theory predicts for a point source of energy that the shock should be parabolic or

$$\frac{y}{d} = k \left(\frac{x}{d} \right)^5 \quad (16)$$

⁺ In the ballistic range case pictures supplied by Dr. Slattery of Lincoln Lab facilitated in checking the calculations.

Van Hise (7) through a characteristics study demonstrated that for a hemisphere nose at high Mach numbers the exponent is slightly less than 0.5. Seiff (8) and Whiting point out from experimental range firings of sphere-cones that one can talk about three shock shape regions, two of which can be approximated by an equation of the form of Eq. (16), but each with different exponents. Considering even more detail for sphere-cones if the body is sufficiently slender, five regions can actually be said to exist. This is seen from Fig. 4 in which the entropy is plotted (or shock strength) vs. radial shock location in nose radii. The five regions are

- 1) high entropy, spherical nose segment which exists until the last characteristic from the sphere intersects the shock
- 2) undershoot and recompression around initial cone section
- 3) conical segment if the body is long enough
- 4) decay starting with intersection of cone shoulder Mach wave and shock
- 5) asymptote downstream where shock approaches a Mach wave.

In Fig. 4 the decay regions for a sphere and two sphere cones ($R_N/R_B = 1/2, 1/12$) are shown. The relative length of the cone segment (or nose/base radius) determines when the expansion fan begins. For the sphere entropy decays smoothly from the nose area. For $R_N/R_B = 1/2$ the shoulder expansion fan "catches" the shock at the limit of the over expansion region and initiates the decay there. For $R_N/R_B = 1/12$ the shock has become asymptotic to a conical shock before the 70 nose radii position. If the body were an ideal pure cone the shock would be constant in strength until the shoulder expansion started. The axial shock coordinate corresponding to the shock position is written along the curve.

The bow shock shapes for all the bodies considered have been plotted in the more conventional manner of $\frac{y_s}{d}$ vs. $\frac{x}{d}$ in Figs. 5 - 8. Fig. 5 shows the results for the spherical nose bodies (Cases I - IV) while Fig. 6 is for the pure cones (Cases A - D). Fig. 7 includes the two low Mach number cones (Cases E, F) as well as that for $M_\infty = 22$, $\theta_c = 12^\circ$ (Case D) for comparison. Finally Fig. 8 compares Case II with a ballistic range shot by Sommer (9) at Ames.

In Fig. 5 the sphere (Case I), which is the same as used before in Ref. (1), gives a straight line with slope $n_1 = .466^+$ which is close to the value obtained when extrapolating to higher Mach numbers from the data of Seiff (8) and Whiting. The sphere-cone (Case II) has a break in the curve at $\frac{x}{d} = 3.7$ due to the initial effects of the cone section⁺⁺. Although the initial segment (spherical) of the sphere-cone has $n_1 = .466$, the latter part has $n_2 = .541$. This bears out a fact which will occur consistently here and was mentioned by Vaglio-Laurin (10) and Bloom, namely that as the drag coefficient of the bodies becomes smaller this decay exponent increases. In fact for Case III (sphere-cone, $R_N/R_B = 1/12$) $n_2 = .613$.

Case III serves to illustrate two other points. First is the far downstream approach to a Mach wave which begins at about $\frac{x}{d} = 30$. Eventually the line would be 45° on this plot and $n_2 = 1$. This region is also seen in Case IV which is the comparison of a sphere fired in a ballistic range at $M_\infty = 9.85$ by Seiff (8) and Whiting and present characteristics calculations.

The second point is that the shock becomes nearly conical along the body and remains so until the corner expansion hits the wave. This is clearly seen for the four pure cones (Cases A - D) shown in Fig. 6.

The fact mentioned earlier about the increase in the exponent n as drag decreases is noticed for the cones here with $n_2 = .523$ for $\theta_c = 32^\circ$ increasing to $n_2 = .613$ for $\theta_c = 12^\circ$. The progression of this slope has been plotted vs. cone angle for the cones in Fig. 9 and vs. drag coefficient in Fig. 10. It is seen to be nearly linear for both these parameters. Sphere and sphere-cone data from the present calculations and Refs. (8) and (10) have been included in Fig. 10. The sphere cone exponents for bodies with drag coefficients between $C_D = 0.27$ and 0.48 seem to be consistently below the pure cone calculations, while the sphere data are almost in line with the cone calculations.

⁺ n_1 denotes slope in nose region, n_2 denotes slope in wake region of bow shock, and n_w denotes wake shock slope.

⁺⁺ On Figs. 5 and 6 the short vertical line along the curves (marked I) denotes the shoulder position for that particular body while the diagonal line (\searrow) denotes position of first shoulder expansion wave intersection with the shock.

Another feature which will turn out to be important regarding the cone turbulent wake behavior is the amount of mass passing through the constant strength portion of the shock, i.e., the position of the shoulder expansion wave-bow shock intersection. This position denoted $(Y_{L_{se}})^+$ has also been plotted in Figs. 9 and 10 and it is seen that the decay exponent n_2 and $Y_{L_{se}}$ behave similarly.

At very large angles of high drag coefficients $Y_{L_{se}}$ has to approach an asymptote because $Y_{L_{se}}$ cannot be less than 0.5. The point at $C_D = 1.51$ in Fig. 10 is from a 60° cone calculation taken from Vaglio-Laurin (10) and Bloom. The individual scattered data shown in Fig. 9 are for the low-Mach number experimental data runs.

Fig. 7 shows the low Mach number runs for the pure cones. Again n_2 increases as cone angle decreases and also as the Mach number decreases. For $M_\infty = 5.9$ and $\theta_c = 12.5^\circ$ the shock is always very weak, in fact on the plot it scarcely deviates from a 45° line. This case gives $n_2 = .816$.

The experimental data of Sommer (9) shown in Fig. 8 was the only experiment available on a slender shape at high Mach numbers. This body was fired at $M_\infty = 17.95$ and is compared here with the calculated shape for the sphere cone at $M_\infty = 22$ ($R_N/R_B = 1/2$). Although the experiment was at a slightly lower Mach number and $\theta_c = 12.5^\circ$ it is felt the agreement is good.

Finally, all the shock waves computed were plotted against the normalizing factor $\frac{x}{\sqrt{C_D}}$ in Fig. 11. For high Mach number the downstream decay portions of the shocks collapse into a fan all passing through $\frac{y_s}{d} = 1.26$ and $\frac{x}{\sqrt{C_D}} = 2.0$. In the nose portion of the shock the curves deviate, indicating the difference between conical type growth and spherical nose shock growth.

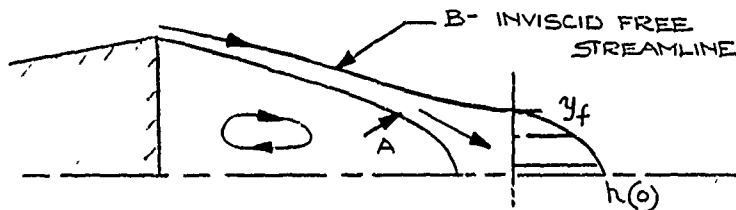
+ For slender cones the Howarth coordinate in the inviscid wake downstream for a given enthalpy level is very nearly equal to the physical coordinate where that particular streamline entered the bow shock since

$$\text{Mass} = \rho_\infty u_\infty \pi y_s^2 = 2\pi d^2 \int_0^{\tilde{y}} \rho u \tilde{y} d\tilde{y} = 2\pi \rho_\infty d^2 \int_0^{Y_L} u Y_L dY_L$$

and at p_∞ , $u_\infty \sim 1.01 u$ then $\frac{y_s}{d} \approx Y_L$.

4. BASE AND NECK PROPERTIES

Before a further determination of the inviscid flow field it is necessary to examine the details of the viscous base and neck regions. This was done only approximately since no complete analysis exists⁺. It was assumed the flow is as postulated by Chapman as shown in the sketch below



Sketch 1. - Base and Neck Region

with a recirculating region and a dividing streamline (A) which stagnates on the axis. The dividing streamline is imbedded in the viscous portion of the flow and separates the recirculating flow from that which passes on downstream. The base pressure, free shear layer, neck size and initial wake pressure are all related. Chapman (11), Kuehn and Larson give the pressure rise at the rear stagnation point in the viscous portion of the flow along the dividing streamline. This pressure rise is a function of the inviscid external Mach number (along B) and the velocity $u^* = \frac{u}{u_\infty}$ along the dividing streamline (A)⁺⁺. To

⁺ Since the following procedure is rather detailed and some of it is accepted to be approximate, the question arises as to how much does the downstream wake depend on the accuracy of the initial quantities. This was considered somewhat in Ref. (1) and will be again in Section 6.4 for the present calculations.

⁺⁺ It is assumed that the flow is brought to rest isentropically at the rear stagnation point from its velocity u^* .

find the correct base pressure the shoulder expansion angle can be changed (which then changes u^* and thus calls for an iteration procedure) until the inviscid pressure behind the shock agrees with the viscous value. The free shear layer properties, giving u^* , will be discussed in Section 4.1.1. One difficulty in carrying out the above procedure in axi-symmetric flow is that the inviscid free streamline is not straight (see Section 4.1.2), thus the necessary inviscid pressure ratio to turn the flow parallel to the wake axis varies depending on the neck thickness. Although the free shear layer properties were examined and the Chapman type procedure was attempted, it is recognized that only a rough answer could be obtained because of the approximations necessary to find u^* and the unknown neck thickness. However, once acceptable values for these quantities are found along with the pressure behind the wake shock properties of the initial wake viscous core can be found directly (Section 4.2).

4.1. Free Shear Layer

We now consider the free shear layer in order to find the dividing streamline velocity u^* and secondly to examine the effects of curvature of the inviscid free streamline in this region.

4.1.1. Velocity Along Dividing Streamline

Chapman (12) has analyzed the free shear layer problem where the initial boundary layer thickness was assumed to be zero. For this case he finds a value of $u^* = 0.58$. Denison (13) and Baum have recently re-examined the Chapman problem with an initial boundary layer thickness and find corrected values of u^* . They, however, do not take into account the facts that the body has a finite height and the distortion in the free shear layer profile caused by the expansion off the body shoulder. Hammitt (14) did the same type of analysis in a more approximate manner assuming an initial cosine shoulder profile. His final results which are given in Fig. 12 are used here. Fig. 12 gives the velocity along the dividing streamline, u^* , as a function of the Chapman mass parameter⁺ ζ and a

⁺ $\zeta = \frac{\Psi}{ux} \sqrt{\frac{R_{ex}}{C}}$ and is zero for the present along the dividing streamline. This can be considered a mass injection parameter where $\zeta < 0$ denotes mass injected resulting in $u < u^*$ ($\zeta = 0$) as shown in Fig. 12.

mixing parameter ξ where

$$\xi = \left(\frac{l}{\delta_{i,1}} \right)^2 \frac{C}{Re_l} \quad (17)$$

and l is length of mixing run, $\delta_{i,1}$ is the initial transformed incompressible boundary layer thickness, C the Chapman viscosity constant and the Reynolds number is the local free shear layer value based on l . The $\xi = \infty$ limit for ($\zeta = 0$) does not correspond to the Chapman value of $u^* \approx 0.6$ but rather gives a value of $u^*(\xi = \infty) = 0.68$ due to the approximations made. These results can then be used to find a correction factor to be applied to the Chapman value.

Detailed calculations using Eq. (17) and Fig. 12 to determine the velocity along the dividing streamline were made for one high Mach number case, namely $R_N/R_B = 1/2$. For the sphere (Case I, Ref. 1) u^* was taken as the Chapman value ≈ 0.6 . As mentioned in regard to the work of Denison (13) and Baum the initial mixing profile after the shoulder expansion off the body is not Blasius-like nor a cosine type. To illustrate the boundary layer velocity and enthalpy profiles before and after the shoulder, as calculated for Case II, are shown in Fig. 13 where the profiles have been expanded around the shoulder by an isentropic stream tube method. The expansion causes the subsonic part of the profile to compress with the result of the flattened profiles as shown. This flattening should have the effect of enhancing the initial mixing and hence raising u^* . For the present a cosine was approximated to the expansion profile of Fig. 12 with the result that $u^* = 0.39$ for Case II at $M_\infty = 22$ and $h_t = 100K$ feet⁺. To find the initial profile after expansion the a priori choice of expansion angle occurs once again, but an error in this choice of several degrees is small compared to the approximation introduced by assuming the profile to be cosine in shape.

⁺ Although it most probably is not correct this same value of u^* was assumed for the pure cone calculations. The effect this has is discussed in Section 4.2.3.

4.1.2. Inviscid Free Streamline

In two dimensional inviscid flow the base free streamline emanating from the shoulder (A in Fig. 3) is straight, but for axis-symmetric flow this streamline curves inward near the axis.

In order to examine this point the shoulder Prandtl-Meyer expansion on the 12° pure cone was set successively at initial expansion angles θ_e of 0° , -2° , -4° , -5° with the horizontal. Fig. 14 shows the trajectories of these streamlines compared with a straight line. For example, for $\theta_e = -4^\circ$ the inclination at $y/R_B = 1/2$ is -6° and approaches -10° near the axis. These angles still result in a long base region, but one effect of interest here is the shock strength required to deflect the streamline back parallel to the axis. As shown on the figure for -4° the difference at this Mach number ($M_e = 17.3$) from -4° to -6° changes p_3/p_2 from 5 to 8.

Thus as mentioned before the size of the neck is now important in determining the pressure ratio p_3/p_2 .

4.2. Initial Core Properties

From Eqs. (11) and (12) it is seen that the initial viscous properties of the core which are needed are the turbulent front location, $(Y_{L_f})_1$, drag in the core, $(C_{D_f})_1$, the axis enthalpy, $\left(\frac{h(0)}{h_\infty}\right)_1$ and the initial pressure level, $\left(\frac{p(0)}{p_\infty}\right)_1$. The pressure is obtained from the characteristics calculations once the base and neck details are prescribed, and is given in Section 5.1. The other three quantities are related through Eqs. (8) and (10) where

$$\left(\frac{\rho_f}{\rho_\infty} \cdot Y_{T_f}\right)^{m+1} \left[\frac{h(0) - h_f}{h_\infty}\right] \cdot G_{m+1} = C_{D_f} \quad (18)$$

⁺ Remembering that $\rho_f/\rho_\infty \cdot Y_{T_f}^{m+1} = Y_{L_f}^{m+1} - \delta(\text{constant})$.

or in the form of Eq. (12b). Thus it is really necessary to calculate independently two of the input quantities. Two procedures were followed depending on the situation. First, where a picture of the neck region was available $(Y_{L_f 1})^+$ was obtained from the picture and independently the initial drag $(C_{D_f 1})$ was calculated. Knowing these two resulted in a value of $h(0)_1$ from Eq. (18) or (12b). However, for most cases, in the absence of a picture $(C_{D_f 1})$ and $h(0)_1$ were estimated, and a check was made by Eq. (18) or (12b) to insure that a reasonable value of the physical $y_{f 1}$ occurred.

4.2.1. Initial Core Drag, $(C_{D_f 1})$

The core drag is assumed to be made of two parts: the skin friction on the body and the drag associated with the pressure rise in the second shock. The latter is found easily once the wake pressure distribution (Section 5.1) is found (1) by $(\Delta D_f)_1 = \pi y_{neck}^2 (p_3 - p_2)$ for axi-symmetric bodies.

Since $(C_{D_f 1}) = (C_{D_f skin}) + (\Delta C_{D_f 1})$ the values used for the present in each case for $(\Delta C_{D_f 1})$ can be found by referring to Tables I and II where all values of $(C_{D_f 1})$ and $(C_{D_f skin})$ are listed. Since the pressure level in the free shear layer base region for a blunt body is usually several times ambient, whereas the slender body is below ambient, $(\Delta C_{D_f 1})$ for the blunt body is larger than for the slender body. For example the sphere at $M_\infty = .22$ and $ht = 100K$ feet has $(\Delta C_{D_f 1}) \cong .0057$ while

⁺ On a picture the physical $y_{f 1}$ is measured. Section 4.2.2 discusses the transformation to $(Y_{L_f 1})$.

for the 12° cone $(\Delta C_{D_f})_1 = .0018$.

Skin friction for pure cones as a function of cone angle is shown in Fig. 15⁺. This was found with the following relation which holds for conical flow:

$$(C_{D_f})_{\text{skin}} = \frac{4}{\sqrt{3}} \frac{\rho_1 u_1^2}{\rho_\infty u_\infty^2} \frac{K''}{\sqrt{R_{e_1}}, R_B} \frac{1}{(\sin \theta_c)^{\frac{1}{2}}} \cos \theta_c \quad (19)$$

$$\text{where } K = K'' \left(\frac{h_c}{h_1}, \frac{u^2}{h_1} \right) \approx .67 \rightarrow .40 \quad (\text{Ref. 15})$$

Initially there were two questions regarding the cone skin friction. First, for small cone angles the cone becomes very long and $(C_{D_f})_{\text{skin}}$ should become quite large. The question was whether this occurred at cone angles of practical interest. Fig. 15 shows that the significant increase in $(C_{D_f})_{\text{skin}}$ begins to occur at very low angles, in fact, below one degree in cone angle. Second was whether, since the inviscid drag is much less for a slender cone, would the skin friction now become larger and in fact dominant. Considering a one foot radius body and angles around 10° at 100K feet altitude the laminar friction drag is still small compared to the pressure drag. If the body were small, or the pressure lower (altitude higher) this would no longer be true. For a body radius of $1/4''$ and 10° cone at 100K feet altitude the friction is over one half the value of the pressure drag.

4.2.2. Turbulent Front Location

The relation between the physical location and transformed location is given by Eq. (12c)

$$\left(\frac{p(o)}{p_\infty} \right)^{\frac{1}{m+1}} \frac{\tilde{y}_f}{Y_{L_f}} = \left[1 + \frac{(m+1) H}{Y_{L_f}^{m+1}} \int_0^{Y_{L_f}} g(Y_{L_f}) d Y_{L_f} \right]^{\frac{1}{m+1}} \quad (12c)$$

⁺ The pressure drag curves shown in Fig. 15 will be discussed in Section 5.2.

so if the physical \tilde{y}_f is read from a picture y_{L_f} is found directly by iterating to get a solution of Eq. (12c) using the appropriate pressure.

Pictures of the neck details are often available (as those given us by Dr. Slattery) for ballistic range shots. However, pictures of the neck details for higher Mach number flows especially for the slender bodies, do not exist. Empirical correlations of neck thickness such as in Ref. (16) do exist, but in general they are not reliable enough to be extrapolated.

4.2.3. Initial Axis Enthalpy Level

The initial value of the axis enthalpy was estimated in Ref. (1) by assuming a rear stagnation point exists at the wake neck and determining the stagnation enthalpy on the stagnated streamline. This stagnated streamline is the dividing streamline considered previously. The recompression of this streamline to zero velocity on the axis is assumed to occur rapidly without any energy loss. To find the stagnation energy along the dividing streamline it is necessary only to find u^* since

$$\frac{\bar{H}}{\bar{H}_\infty} = \left(1 - \frac{h_w}{\bar{H}_\infty} \right) u^* + \frac{v_w}{\bar{H}_\infty} \quad (20)$$

where \bar{H} is local stagnation enthalpy and h_w is the known wall enthalpy. For a cold wall Chapman's value of u^* would give $h(0)_1 \cong 0.6\bar{H}_\infty$. At hypersonic speeds this is indeed quite hot. This value was taken for the sphere as calculated in Ref. (1). For the case calculated in detail here, Case II, in which $u^* = 0.39$ (Section 4.1.1), $\frac{h_w}{\bar{H}_\infty}$ was taken as 0.13 thus $\frac{\bar{H}}{\bar{H}_\infty} = h(0)_1/\bar{H}_\infty = 0.47$ from Eq. (20).

Rather than repeat this involved procedure for the pure cones the initial $h(0)_1/h_\infty$ value was arbitrarily taken to be

this same value, i.e., $\left(\frac{h(0)}{h_\infty}\right)_1 = 46$ at $M_\infty = 22$. This is most probably not correct, but as shown later it turns out that the cone equilibrium wake behavior is relatively insensitive to the initial enthalpy level. But for the non-equilibrium case an exact determination of this enthalpy level for a slender body is still a most important question.

For the experimental range firings it was not necessary to determine $h(0)_1$ independently, since usually the direct method of measuring the neck thickness from a picture was used and $h(0)_1$ found from Eq. (18). However, for these cases values of $h(0)_1/\bar{H}_\infty \approx 0.5$ always occurred.

4.3. Wake Shock

With the shoulder expansion angle and the neck thickness determined the wake shock can now be inserted in the inviscid flow. To review, the characteristics calculations were made for the geometry shown in Fig. 3 where A is a constant pressure free streamline and B is an inserted cylindrical sting. The resulting wake shock shapes are shown in Figs. 5 and 7. These include both the high Mach number results and those for the experimentally fired cones. The nose is so small for $R_N/R_B = 1/12$ that the wake shock is taken to be the same as the pure cone (Case D). Initially each of these wake shocks travel outward quite rapidly except for the latter cases (III or D) which seem to take some time for the shock to strengthen. The wake shock approaches the position of the bow shock with $n_w > 1$, and eventually becomes almost parallel with it as both decay to a Mach wave together.

5. PRESSURE DISTRIBUTION, PRESSURE DRAG AND INITIAL WAKE ENTHALPY DISTRIBUTIONS

5.1. Pressure Distribution

The pressure distributions in the nose region and along the afterbody for each of the bodies calculated are shown in Figs. 16-18. Fig. 16 shows the four sphere, sphere-cone cases at $M_\infty = 10$ and 22, Fig. 17 the pure cones at $M_\infty = 22$ and Fig. 18 the two experimental

cone cases. The axial coordinate, $\frac{x}{d}$, used in the figures was measured from the apex of the shock in order to keep the coordinates consistent with those for the shock shape. For the most part both a cylindrical and wake afterbody are shown. Again Refs. 7, 10 and 17 present detailed pressure distribution studies for air so only a few comments as to the present particular cases will be made here. First, if the flow at the body shoulder is expanded to be parallel to the free stream⁺ the resulting pressure is not much different from that which will occur behind the wake shock (where the flow is again parallel to the free stream). This is expected since the wake shock is relatively weak. Thus at $M_\infty = 22$ the initial wake pressure for the blunt body is $\frac{p_3}{p_\infty} \approx 24$ while for the slender cone $\frac{p_3}{p_\infty} \approx 1 - 2$. This is one of the fundamental differences between the hypersonic blunt body and slender body. In general, the pressure behind the wake shock for the blunt body is quite high whereas for the slender body it is nearly ambient.

Secondly, the pressure with the wake shock included rapidly approaches the distribution which would exist for the same forebody but with a cylindrical afterbody (instead of wake). In fact by 10 diameters behind the wake shock the pressure is very near to the cylindrical value⁺⁺.

As illustrated in Fig. 17 and pointed out by Vaglio-Laurin (10) and Bloom, the cone-faced bodies at high Mach number exhibit a downstream recompression on the cylindrical afterbodies, which exists consistently for all cone angles considered here. This also is seen from Fig. 17 to exist when the wake shock is inserted (17).

The calculations for the two low speed experimental runs are shown on Fig. 18.

⁺ For a sphere it already is parallel to the free stream at the shoulder.

⁺⁺ This is not true regarding the temperature since any entropy rise persists in an inviscid flow.

5.2. Inviscid Forebody Drag Coefficient (Pressure Drag)

The inviscid drag coefficient for pure cones as a function of the cone angle is shown in Fig. 15 and for various sphere-cone combinations (from Ref. (18)) in Fig. 19.

Previously (1) the drag coefficient for a sphere had been taken as unity. The more detailed characteristics results indicate here a value of $C_{D_0} = 0.94$. Characteristics calculations made presently for the 12° cone are shown as the circled line in Fig. 19. The difference for this one angle is that the calculations were carried very far downstream such that a pure cone was approached ($R_N/R_B \approx .075$). The approach to the slender cone shows that the drag coefficient actually undershoots the cone value by a small amount (19), and that for a value of R_N/R_B as high as 0.2 the drag coefficient is almost the same as for a pure cone. This is due to the pressure undershoot on the cone surface when a small spherical nose is put on the body. Thus it is necessary to blunt the nose a surprising amount before any significant effect on the over-all drag coefficient occurs. This fact will have significance later in determining the wake properties.

5.3. Initial Wake Inviscid Enthalpy Distribution

The inviscid enthalpy distributions downstream at $p = p_\infty$ are shown in Fig. 20 for $M_\infty = 5.9$ and Figs. 21 and 22 for $M_\infty = 22$. The profiles as shown are in the Howarth coordinate which is used in the analysis.

For the case of $M_\infty = 5.9$ the enthalpy both with and without the wake shock is shown in Fig. 20. The bow shock profile is constant until the expansion fan occurs. The sudden change in slope here plays an important role in the wake history. The wake shock contribution is significant near the axis where the flow deflection is the greatest. However, as indicated by the line labeled $(Y_{L_f})_i$ most of this peak is engulfed in the viscous core at the neck. The effect of the second

shock is to "smear" out the vertical front presented by the bow shock. For this low Mach number even the peak inviscid enthalpy at $Y_L = 0$ is relatively "cold", giving only $\frac{h}{h_\infty} = 1.2$. This effect tends toward computational difficulties when computing quantities such as drag which depend on very small differences.

The high Mach number cone shown in Fig. 21 indicates again that most of the "hot" inviscid region due to the wake shock should be already swallowed by the "neck". In this case, to the accuracy of the computations, the wake shock gave no noticeable contribution beyond the knee in the curve ($Y_L > Y_{L_{se}}$). For this cone even at $M_\infty = 22$ and including the wake shock the maximum inviscid enthalpy ($\frac{h}{h_\infty} \approx 3$) is still "cold" compared to the viscous core value used here ($\frac{h(0)}{h_\infty} = 46$).

Primarily shown on Fig. 22 is a compilation of enthalpy profiles for $M_\infty = 22$ including both families of sphere-cones and pure cones. For $R_N/R_B = 1/12$ the extremely small hot pulse (normal shock enthalpy expanded to $p = p_\infty$) occurs because of the small nose radius. The overshoot on the cone region of the shock shape as discussed earlier is evident here by the dip in the enthalpy profile, followed by the approach to the cone value at $Y_L = 0.4$. Boundary layer calculations at the cone shoulder show that the mass in this inviscid hot pulse is entirely engulfed in the boundary layer by that point, thus it is incorrect to carry it into the wake calculations. In fact, as shown on Fig. 22 the enthalpy undershoot is also within the viscous region at the time the flow reaches the neck. Thus if the nose/base radius ratio is as small as $1/12$ pure cone flow can be used for equilibrium wake calculations.

For $R_N/R_B = 1/2$ the width of the inviscid enthalpy pulse has been reduced from the sphere by a factor of 2-3 which is certainly predictable from the drag coefficients. Here the viscous front is

still within a very hot region but near the point of rapid change. This will effect the nature of the wake history as seen later.

Besides the 12° cone Fig. 22 shows pure cone enthalpy profiles for $\theta_c = 22^\circ$ and 32° . From these curves comparing the general nature of the sphere cones and pure cones it can be seen how differently the nose shapes distribute the wake enthalpy. One very vivid comparison is the 22° cone and sphere-cone ($\theta_c = 12^\circ$, $R_N/R_B = 1/2$), which have the same over-all drag but from Fig. 22 are seen to be very much different in distribution.

In conclusion the inviscid flow field can be affected drastically by shaping the body. We now turn our attention to the calculation of the downstream wake properties.

6. DISCUSSION OF DOWNSTREAM WAKE PROPERTIES

In order to find the downstream wake properties Eq. (11) along with its component parts has been programmed on a computer. The necessary inputs are the initial values of $(Y_{L_f 1})$, $(C_{D_f 1})$, $\left(\frac{h(0)}{h_\infty}\right)_1$, along with the downstream pressure history, $\frac{p}{p_\infty}$ vs. $\frac{x}{d}$, and the radial enthalpy distribution $g(Y_L)$ vs. Y_L . The enthalpy distribution was put in numerically as determined directly from the shock shape. Previously (1) the distribution was approximated analytically in such a manner as to make the total drag correct. The advantage of using the numerical value is that no distortion of the profile occurs in the sensitive inner portion by forcing an over-all curve fit. Also, if only partial shock shapes are known the wake can be found at least for some distance downstream.

A question occurs concerning the initial axial station at which mixing calculations should be started. This occurs because the analysis does not include a pressure gradient and the pressure drops initially very rapidly, especially for a blunt body. The procedure adopted in Ref. (1) was again used, namely it was arbitrarily assumed no mixing occurs until the pressure is down to $p/p_\infty = 4$. The wake is assumed to simply expand by the square root of the pressure ratio from the neck to the initial mixing station, i.e., where $p/p_\infty = 4$.

Since for a blunt body at high speeds the pressure behind the shock is about $24 p_\infty$ this results, in practice, in starting the mixing calculations 6-8 diameters downstream. For a slender body, however, ($\theta_c \approx 12^\circ$) the calculations are started right at the neck since the pressure is less than $4 p_\infty$ initially.

6.1. Wake Growth

The three features brought out below deal with, 1.) shape variation comparing wakes of blunt and sharp bodies, 2.) shape variation effects on bodies with the same drag coefficient, and 3.) altitude (Reynolds number) effects.

6.1.1. Effect of Shape Variation (Blunt vs. Sharp)

The available experimental wake growth data are from Slattery (4) and Clay and Siperly (5) and Short. A comparison of the theoretical and measured growth for the ballistic range data of Slattery (4) and Clay is shown in Fig. 23. The figure also shows their measurements for spheres and the corresponding calculations made in Ref. (1). The difference in character in the sphere growth and cone growth can be seen. The dotted line is the asymptotic value for the cone calculations and it falls below the sphere calculations by the cube root of the drag ratio. The present theoretical line for the cones is on the low side of the data and is lower than the scatter from $100 < \frac{x}{d} < 1,000$. The theoretical inflection point around $\frac{x}{d} = 600$ is the point at which the front breaks out into flow coming through the expansion region of the shock and the drag (as small as it is) is engulfed rapidly. It would appear something like this happens around $\frac{x}{d} = 100$ in the experiments.

The comparison with the Siperly (5) and Short data is shown in Fig. 24. The data was taken at NASA-Ames. This body is a blunter cone and at slightly higher velocity than the Lincoln data. The data indicates a rather sudden increase in wake width around $\frac{x}{d} \approx 100$. This is the typical behavior predicted for a cone; however, the "explosion" predicted

from the theory occurs later at around $\frac{x}{d} \approx 300$. The early humps in the curves around $\frac{x}{d} \approx 10$ occur due to the pressure decrease to ambient. At $\frac{x}{d} \approx 1,000$ most of the drag should be engulfed by the core and the curves should approach their asymptotic behavior.

Growth curves for three cases at high Mach number are shown in Fig. 25 to illustrate further the contrast between blunt and slender bodies. Those shown here are the 12° cone, sphere-cone, sphere family (Cases I, II and D).⁺

Here again the cone curve is significantly below the other shapes. The sudden explosion at about $\frac{x}{d} \approx 30$ for $R_N/R_B = 1/2$ is due to the previously mentioned fact that the front started in a hot region but very close to a rapid drop off in the enthalpy. The cone wake growth is near a cube root throughout except around $\frac{x}{d} \approx 700$ where it hits the sudden drop in inviscid enthalpy as seen in Fig. 21. The humps in the growth curves for low values of $\frac{x}{d}$ (< 50) are again due to the pressure decay characteristics.

The rate of turbulent core growth depends on the amount of inviscid drag swallowed. In fact, over the whole regime a rough qualitative estimate (1) states that for an axi-symmetric wake

$$Y_{T_f}^3 \sim K C_{D_f} (Y_{T_f}) \frac{x}{d} \quad (21)$$

If Eq. (21) is normalized by $\sqrt{C_D A}$, where A is the base area, then (2)

$$\frac{Y_{T_f}}{\sqrt{C_D A}} \sim K \left[\frac{x}{\sqrt{C_D A}} \frac{C_{D_f} (Y_{T_f})}{C_D} \right]^{1/3} \quad (22)$$

⁺ Base radius R_B was taken as 1 Ft.

The only difference from a low speed wake is that $C_{D_f}(Y_{T_f})$ is a changing function except in the constant conical region for a cone and the far downstream asymptote where $C_{D_f}(Y_{T_f})/C_D = 1.0$ (See Eq. 9).

For the early stages of the cone growth, rather than an approximate equation of the form of Eq. (22), the full Eq. (11) can be simplified considerably. As long as the turbulent front for the cone is growing into a uniform region, which is "cold", no relative drag compared to the initial front is being engulfed. For the cone up to the point where the front begins to decrease $g(Y_L) = 1$, $\frac{h_f}{h_\infty} = 1 + H$ and from Eq. (12c)

$$\left(\frac{p(0)}{p_\infty}\right)^{\frac{1}{m+1}} \frac{\tilde{y}_f}{Y_{L_f}} = \left[1 + H\right]^{\frac{1}{m+1}} \quad (12c)$$

Also, since the slope of the front is zero and no relative drag has been engulfed, $F_1 = F_2 = 1$. With these facts Eq. (11) becomes

$$\int_{Y_{L_f i}}^{Y_{L_f}} (Y_{L_f}^{m+1} - \delta) \left(\frac{h(0)}{h_\infty}\right)^{\frac{1}{m+1}} dY_{L_f} = \text{Const.} (C_{D_f})_i \int_{\left(\frac{x}{d}\right)_i}^{\frac{x}{d}} \left(\frac{p(0)}{p_\infty}\right)^{\frac{1}{m+1}} d\left(\frac{x}{d}\right) \quad (11')$$

The axis enthalpy is now $\frac{h(0)}{h_\infty} = (1+H) + \frac{\text{const.}}{Y_{L_f}^{m+1} - \delta}$, so Eq. (11')

becomes

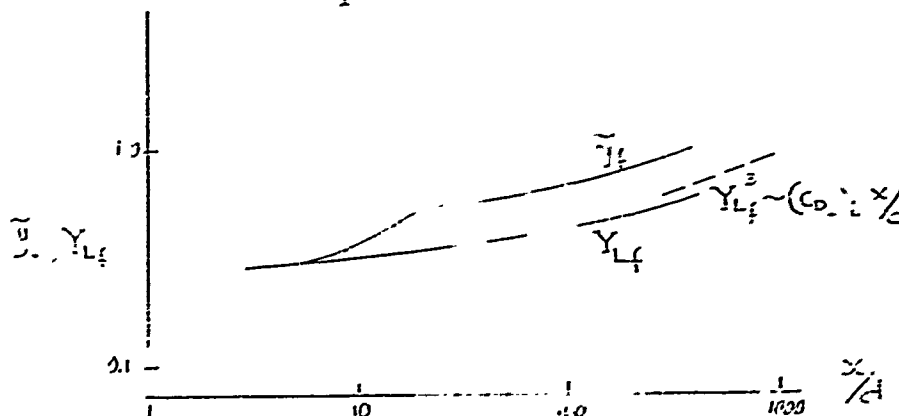
$$\int_{Y_{L_f i}}^{Y_{L_f}} (Y_{L_f}^{m+1} - \delta) \left[(1+H) + \frac{\text{const.}}{Y_{L_f}^{m+1} - \delta} \right]^{\frac{1}{m+1}} dY_{L_f} = \text{const.} (C_{D_f})_i \int_{\left(\frac{x}{d}\right)_i}^{\frac{x}{d}} \left(\frac{p(0)}{p_\infty}\right)^{\frac{1}{m+1}} d\left(\frac{x}{d}\right) \quad (11'')$$

The axis enthalpy term in the [] brackets has the effect of slowing down the initial growth, but becomes small, fairly soon

and when $Y_{L_f}^{m+1} \gg \delta$, $Y_{L_f}^{m+2} (C_{D_f})_i \cdot \frac{x}{d}$ similar to Eq. (21).

Thus as $h(0) \rightarrow h_f$ and prior to reaching the break in the enthalpy curve the cone growth should go as the cube root and be nearly proportional to $(C_{D_f})_i$. This is shown for Y_{L_f} in the sketch below

which is taken from the calculations for the 12° cone at $M_\infty = 22$. The physical \tilde{y}_f is also shown. The varying difference between \tilde{y}_f and \tilde{y}_{L_f} is because of the pressure history.



Sketch 2. Initial Cone Wake Growth

At the far downstream asymptote where all the drag has been engulfed by the turbulent core Eq. (11) becomes

$$\tilde{y}_f^{m+2} = - (m+2) \frac{K}{\beta^2} \frac{G''(0)}{4^{m+1} G_{m+1}} (C_D) \frac{x}{d} \quad (23)$$

which when normalized with $\sqrt{C_D A}$ becomes like Eq. 22 where

$$C_{D_f} (y_{f_f}) / C_D = 1.0$$

$$\left[\frac{y_f}{\sqrt{C_D A}} \right]^3 = \text{Const.} \frac{x}{\sqrt{C_D A}} \quad (24)$$

Thus plotting the wake growth normalized by $\sqrt{C_D A}$ gives one curve asymptotically for all bodies regardless of shape and size. This is shown in Fig. 26.

6.1.2. Effect of Shape Variation (Same Drag Coefficient)

The blunted cone $R_H/R_B = 1/2$ and the 22° pure cone have the same drag coefficient ($C_D \cong .30$). The inviscid enthalpy profiles were seen in Fig. 22 to have completely different enthalpy distributions although the drag integral is the same.

From the discussion in the previous section on general blunt vs. slender wake growth one might expect the early portions of the wake of these two bodies to be different and this is seen to be true in Fig. 27. Eventually the curves coincide but until $\frac{x}{d} \approx 1,000$ the behavior for these two bodies of the same drag (and area) is quite different.

6.1.3. Effect of Altitude Variation

The effect due to altitude is caused primarily by the Reynolds number through $(C_{D_f})_1$. In comparing small scale ballistic range data with large body high Mach conditions this effect can be very important. To illustrate, three high Mach cases were calculated at altitudes of 60K, 100K and 150K feet. For the higher altitudes or lower Reynolds number, the skin friction becomes a larger percentage of the total drag. This results in the turbulent core starting farther out on the inviscid front, which in turn tends to reduce the initial growth differences seen to exist previously. Indeed, if $(C_{D_f})_1$ is large enough, all that occurs is the asymptotic cube root growth.

The importance of this effect is seen in Fig. 27, where curves for both 100K and 150K feet are included, and Fig. 28 for the 12° cone. In Fig. 27 the difference between the two bodies is smaller at 150K feet than at 100K feet. In fact, in Fig. 28 for the 12° cone at 150K feet no hump in the curve is observed because the front starts outside of the enthalpy break. The reason that the 60K feet curve is above that for 100K feet is because turbulent skin friction was assumed to exist at this altitude. If transition on the body occurs at an altitude different from what was assumed here, obviously $(C_{D_f})_1$ changes and consequently also the downstream wake.

Ballistic range measurements are made with fairly small bodies at reduced pressure so care must be exercised in choosing the experiments if one is looking for body shape variations.

6.2. Enthalpy and Velocity Distributions

Perhaps the most significant effect of shaping can be seen from the enthalpy and velocity distributions as shown in Figs. 29 and 30. Fig. 29 shows the enthalpy and velocity distributions along the axial streamline and the front for the 12° cone - sphere family (Cases I, II and D). These are plotted against the "reduced" coordinate $\frac{x}{\sqrt{C_D A}}$. Since the analysis assumes a constant stagnation enthalpy $u \sim \sqrt{h - h_\infty}$, and the velocity deficit along the axial streamline normalized by the free stream, $\frac{u_\infty - u(0)}{u_\infty}$, is shown on the right hand ordinate. Fig. 30 shows the enthalpy and velocity distributions along the axial streamline at two altitudes for the two bodies with the same drag (Cases II and B).

It is noted that reducing the nose radius significantly reduces the wake temperatures, especially for the cone which drops an order of magnitude faster than the sphere. In fact the cone drops so rapidly it appears the very early history is insensitive to the exact initial enthalpy level chosen. This general behavior is not evident beforehand because the front spreading rate is much slower for the cone. Conceivably the low cone wake growth rate could cause any high core temperatures to persist far downstream. The long persistence of a high core temperature is enhanced by and, in fact, depends on the core engulfing hot fluid or drag from the outer region. For an axi-symmetric body the enthalpy excess of the axis above the front is given by Eq. (8) or (18)

$$\frac{h(0) - h_f}{h_\infty} \sim \frac{C_{Df}}{y_{1f}^2}$$

where C_{D_f} is the initial plus engulfed drag in the core. If the momentum defect relative to the front increases, then C_{D_f} increases with Y_{L_f} thus keeping $(h(0)-h_f)$ large. For the sphere this occurs such that $(h(0)-h_f)$ is almost constant for hundreds of diameters, and the overall temperature level drops only as the front temperature decreases which is relatively slow. For the cone practically no inviscid drag relative to the initial front is engulfed for hundreds of diameters (the inviscid enthalpy profile is almost constant), thus any core expansion at all has directly the effect of drastically reducing the temperature.

The velocity follows a similar history. For the cone the velocity is only 5% different from free stream by 125 units of

$$\frac{x}{\sqrt{C_{D_f} A}} \quad (\sim 30 \text{ body diameters}), \text{ whereas for the sphere it takes nearly } 650 \text{ units of } \frac{x}{\sqrt{C_{D_f} A}} \quad (\sim 600 \text{ body diameters}).$$

Another interesting comparison deals with the velocity slowdown at some level of radar frequency, say UHF (n_e (critical) $\sim 1.6 \cdot 10^9$ electrons/cm³). At this point for the sphere a change in velocity of 100 ft./sec. would occur in a distance of $\Delta x \sim 25$ feet (assuming $d = 2$ feet) while for the cone $\Delta x \sim 1$ foot.

In comparing the enthalpy and velocity histories of the two bodies with the same drag (Fig. 30, Cases II and B), it is seen they are quite different, as were the wake growths. The 22° cone follows more closely the drop of the 12° cone rather than the blunt body. Also, as in the wake growth, the effect of increasing $(C_{D_f})_1$ (raising the altitude) decreases the difference between the bodies.

6.3. Electron Decay

6.3.1. Equilibrium Flow Conditions

The effect of the drop in enthalpy with decrease of

nose bluntness is felt directly on the electron decay as shown in Fig. 31. This shows the axial electron density for the 12° cone, sphere-cone and sphere (Cases D, I and II). Both the cone and sphere-cone electron concentrations drop rapidly in comparison to the sphere.

The dependence of the equilibrium electron concentration on drag coefficient for this class of bodies, i.e., sphere- 12° cone series, can be seen by cross plotting the distance it takes to drop to various electron levels vs. the drag coefficient. This is shown in Fig. 32 where the electron levels have been arbitrarily chosen as those corresponding to critical frequencies for C band (5600 mc), L band (1300 mc), and UHF (400 mc). The surprising result occurs that the decay length is linear with the drag coefficient. In view of the other results concerning bodies with different cone angles this curve cannot be applied to any general shape. It should, however, hold for other sphere-cone bodies with a 12° cone angle.

6.3.2. Pure Mass Diffusion

The electron decay for pure diffusion is also shown in Fig. 31 for the cone and sphere. This calculation makes use of Eqs. (14) and (15) and assumes a foreign species (e.g., ablation products) to be deposited into the wake through the neck with an initial gaussian radial distribution and subsequent zero recombination. The diffusivity used is that which is found for the enthalpy. Fig. 31 shows this type of diffusion for the cone to be even slower than for the sphere. Since no recombination takes place, the slow diffusion results from the slow cone wake growth. Very far downstream, after the "explosion" in cone growth the rate will eventually be the same.

Except for the pure diffusion calculations of this section the assumption of thermodynamic equilibrium has been made everywhere in this report. This means that as far as an

application to the re-entry problem is concerned the results will not hold above a certain altitude, which is approximately 100K feet (see Ref. 2) due to non-equilibrium effects. The possible importance of non-equilibrium effects is emphasized by the results of Fig. 31 in noting the difference between the equilibrium curve on the one hand and the ultra-conservative zero recombination pure diffusion on the other hand.

6.4. Effect of Accuracy of Initial Wake Conditions

An effect of inaccurately choosing the initial conditions for the wake can be inferred either from the enthalpy histories or the wake growth curves in Fig. 27. For the sphere-cone ($R_N/R_B = 1/2$) the difference in (C_{D_i}) at 100K feet and 150K feet is almost exactly a factor of two. Beyond the relative differences in wake behavior discussed previously, it is noted that the basic nature does not change due to this difference in initial conditions. Also the cone enthalpy histories of Fig. 30 show very little difference between the 100K feet and 150K feet conditions and the (C_{D_i}) variation for these is about 2.5. Thus it appears that on an absolute basis the error must be fairly large before any fundamental difference in wake behavior would occur.

7. CONCLUSIONS

1. The analysis of Ref. 1 can be applied to slender bodies as well as blunt bodies.
2. Body shaping has only a small effect on initial core drag values, these being nearly equal for the sphere and cone of the same base diameter. The Reynolds number of the body (size or pressure) is much more significant in determining the initial core drag.
3. The wake shock may alter the shape of the inviscid enthalpy profile significantly for slender bodies (especially at low Mach number), but does not alter the wake growth to any degree. This is because the general level of the inviscid enthalpy is so low.

CONCLUSIONS (Cont'd.)

4. The turbulent front growths behind the cones calculated are slower than for blunt bodies until $\frac{x}{\sqrt{C_D} \Lambda} \approx 10^4$.
5. Axial enthalpies drop very rapidly as the nose is sharpened. Slender cone wake enthalpies decrease an order of magnitude faster than the sphere.
6. Bodies of the same drag coefficient but different shapes will have different wake histories until the asymptotic downstream conditions are reached.
7. An increase in core drag or altitude tends to decrease any difference in wake behavior due to shaping.
8. Equilibrium electron density decay follows the fast drop of the enthalpy with nose sharpening. It was found for the sphere -12° cone family of bodies that the axial distance to decay to a given electron density was directly proportional to the drag coefficient. However, this behavior is not a unique function of the drag coefficient for all body shapes.
9. Until significant inviscid wake drag is engulfed the slow cone wake growth can cause the pure diffusion of a foreign species (e.g., ablation products) with zero recombination deposited in the wake to take even longer for the cone than the sphere.

ACKNOWLEDGEMENTS

The authors wish to express their appreciation to Dr. A. Hammitt for many helpful discussions during the course of the work, to Mr. A. Maddox for assisting in the calculations and Mr. W. Buck for running the computer program. We also wish to thank Mr. S. C. Sommer of NASA for use of his unpublished data.

REFERENCES

1. Lees, L. and L. Hromas, "Turbulent Diffusion in the Wake of a Blunt-Nosed Body at Hypersonic Speeds", IAS, Vol. 29, No. 8, August, 1962.
2. Lees, L., "Hypersonic Wakes and Trails", Paper to be presented at ARS national meeting, Los Angeles, California, November 13 - 18, 1962.
3. Bloom, M., "Thermal and Chemical Effects in Wakes", Paper presented at AGARD meeting on High Temperature Aspects of Hypersonic Flow, Brussels, Belgium, April, 1962.
4. Slattery, R. E., and W. Clay, "Experimental Measurement of Turbulent Transition, Motion, Statistics and Gross Radial Growth Behind Hypervelocity Objects", MIT Lincoln Laboratory, Preprint JA-1891, April, 1962.
5. Siperly, B. and W. Short, Convair Division of General Dynamics, Private Communication.
6. Feldman, S. and A. Widawski, "Errors in Calculating Flow Fields by the Method of Characteristics", ARS Journal, Vol. 32, No. 3, P. 434, March, 1962.
7. Van Hise, V., "Analytic Study of Induced Pressure On Long Bodies of Revolution with Varying Nose Bluntness at Hypersonic Speeds", NASA TR R-78, 1960.
8. Seiff, A. and E. Whiting, "A Correlation Study of the Bow-Wave Profiles of Blunt Bodies", NASA TN D-1148, February, 1962.
9. Sommer, S. L., NASA Ames, Private Communication.
10. Vaglio - Laurin, R. and M. Bloom, "Chemical Effects in External Hypersonic Flows", ARS, Paper presented at International Hypersonic Conference, MIT, August, 1961.
11. Chapman, D. R., Kuehn, D. and H. Larson, "Investigation of Separated Flows in Supersonic and Subsonic Streams with Emphasis on the Effect of Transition", NACA TR 1356, 1958.
12. Chapman, D. R., "Laminar Mixing of a Compressible Fluid", NACA Rep. 958, 1950.
13. Denison, M. R. and E. Baum, "Free Shear Layer with Finite Initial Profile", RN No. 2, Electro-Optical Systems, Inc., Pasadena, California, March, 1962.
14. Hammitt, A. G., "Effects of the Separated Region on the Heat Transfer and Flow About A Chin Radome Configuration", GASL, Rep. No. 14, November, 1959.

REFERENCES (Cont'd.)

15. Van Driest, E., from "The Dynamics and Thermodynamics of Compressible Fluid Flow, Vol. II", Shapiro, A. H. Ronald Press Co., New York, 1954.
16. Feldman, S. and A. Widawski, from "Research on Base Flow and Wakes (U)", Section 5, Semi-Annual Rep. No. 1810-2Q-1, Electro-Optical Systems, Inc., November, 1961.
17. Wan, K. S., "Inviscid Flow Field in the Wake of Hypersonic Bodies", G. E. - MSVD, TIS R62S020, March, 1962.
18. Thompson, T. R., Space Technology Laboratories, Inc., Private Communication.
19. Chernyi, G. G., "Introduction to Hypersonic Flow", Translated and edited by R. Probst, Academic Press, New York, 1961.

Case	Alt. (000)	M_∞	V_∞	R_N/R_B	θ_c°	$\frac{h(O)}{h_\infty} / i$	$\frac{h_f}{h_\infty} / i$	C_{D_o}	$(Y_{L_f})_i$	$\frac{\gamma_{neck}}{R_B}$	$(C_{D_f})_{skin}$	$(C_{D_f})_i$	$\frac{P_{neck}}{P_\infty}$
I	100	22	22,070.6	1	--	58	36.9	.94	.146 ⁺	.37	.002	.0077	24
II	100	22	22,070.6	1/2	12	46	29.3	.30	.153 ⁺	.55	.0032	.0066	7.8
	150	21.5	23,365.	"	"	"	27.8	"	.202 ⁺	.79	.0097	.0131	"
III	100	22	22,070.6	1/12	12	Reduces to Case D							
A	100	22	22,070.6	0	32		9.65	.60	Inviscid Flow Only				
B	100	22	22,070.6	0	22	46	5.25	.30	.229	.59	.0075	.009	3.17
	150	21.5	23,569.8	"	"	"	5.25	"	.369	.95	.022	.0235	3.17
C	100	22	22,070.6	0	19			.24	Shock and Pressure Only				
D	60	22	21,298.0	0	12	46	2.31	.094	.374	.78	.0115 [*]	.0133	2.15
	100	22	22,070.6	↓	↓	↓	2.45 ^{**}	↓	.289	.62	.0072	.009	↓
	150	21.5	23,569.8				2.31		.515	1.06	.0222	.0240	

+ Corresponds to $\frac{x}{d}$ when $\frac{p(O)}{P_\infty} = 4$

* Turbulent skin friction used

** Calculated with wake shock

TABLE I. Tabulation of Body Parameters - Re-Entry Conditions

CONVAIR-NASA													
Case	P_∞	M_∞	V_∞	R_M/R_B	θ_c°	$\frac{h(o)}{h_\infty} / f_i$	$\frac{h_f}{h_\infty} / f_i$	C_{D_o}	$(Y_{L_f})_i$	$\frac{y_{neck}}{R_B}$	$(C_{D_f})_{skin}$	$(C_{D_f})_i$	$\frac{P_{neck}}{P_\infty}$
E	48 mm	7.82	8,700	0	25		1.67	.39	.264	.515	.0175	.0255	1.75

LINCOLN LAB													
Sphere Ref. 1	40 mm, 1 ATM	8.5	9,500	1	-		4.60	1.0	.229 [†]	.40	.007	.022	8.8
F	.071 ATM	5.9	6,680	0	12.5		1.08	.15 [*]	.308	.54	.0217	.0365	1.44

HUSA													
IV.	.059 ATM	10.0	9,680.8	1	-			1.0					Inviscid Flow Only

+ Corresponds to $\frac{x}{d}$ when $\frac{p(o)}{p_\infty} = 4$

* Includes base drag

TABLE II. Tabulation of Body Parameters - Ballistic Range Conditions

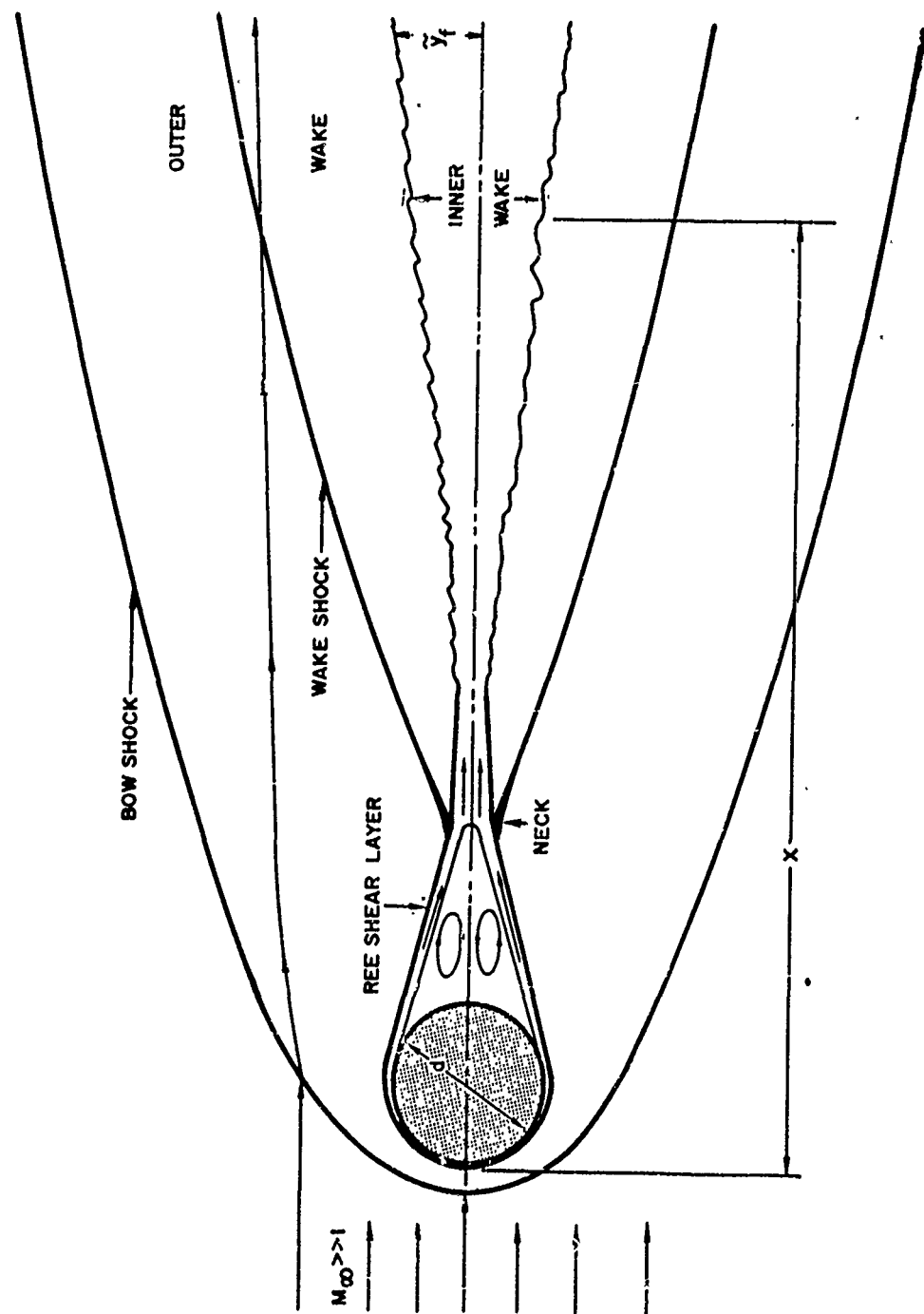
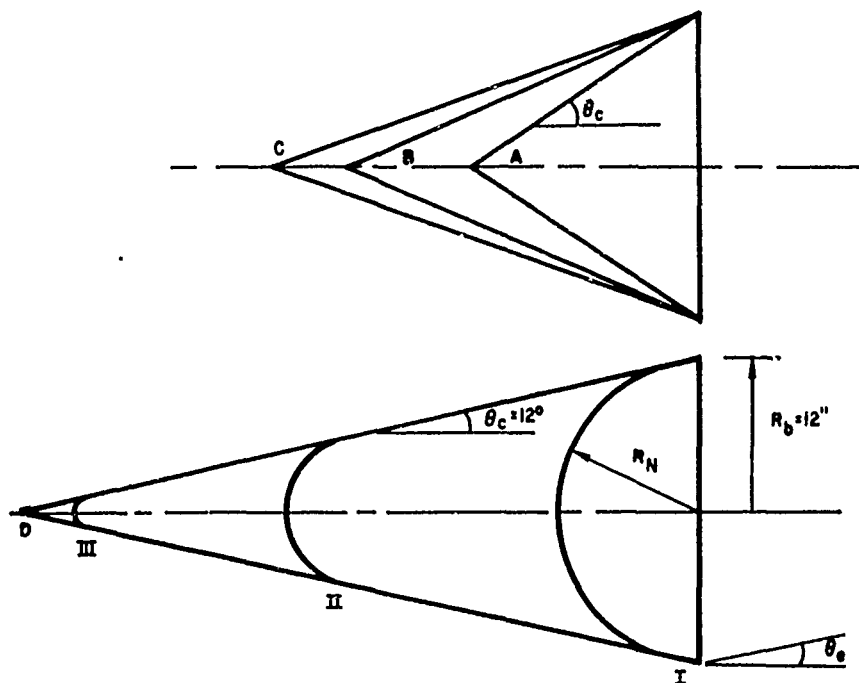


Figure 1. Wake Behind Blunt Body at Hypersonic Speeds



BODY NOSE/BASE RADIUS

I	1 (HEMISPHERE)
II	1/2
III	1/12
A	0 (CONE) $\theta_c = 32^\circ$
B	0 " $\approx 22^\circ$
C	0 " $\approx 19^\circ$
D	0 " $\approx 12^\circ$

Figure 2. Body Geometry Schematic

A FREE STREAMLINE BOUNDARY ($\rho = \text{CONSTANT}$)
 B CYLINDRICAL STING

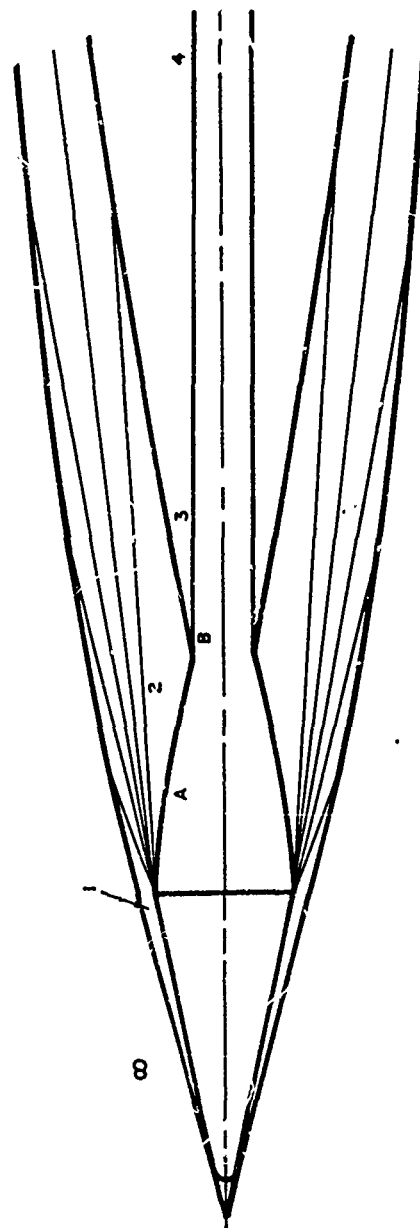


Figure 3. Inviscid Flow Configuration for Slender Body

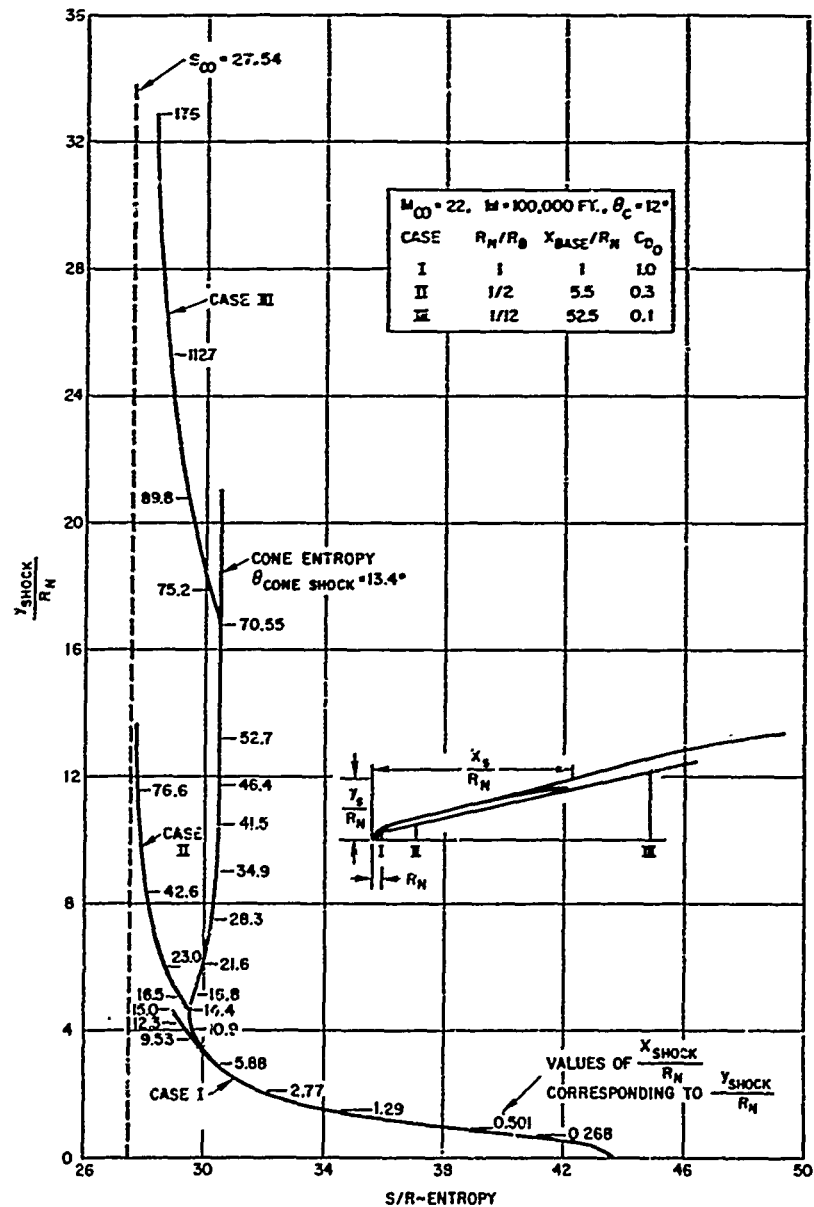


Figure 4. Bow Shock Wave Characteristics for Various Sphere-Cone Combinations ($M_{\infty} = 22$, $h = 100,000$ ft., $\theta_c = 12^\circ$)

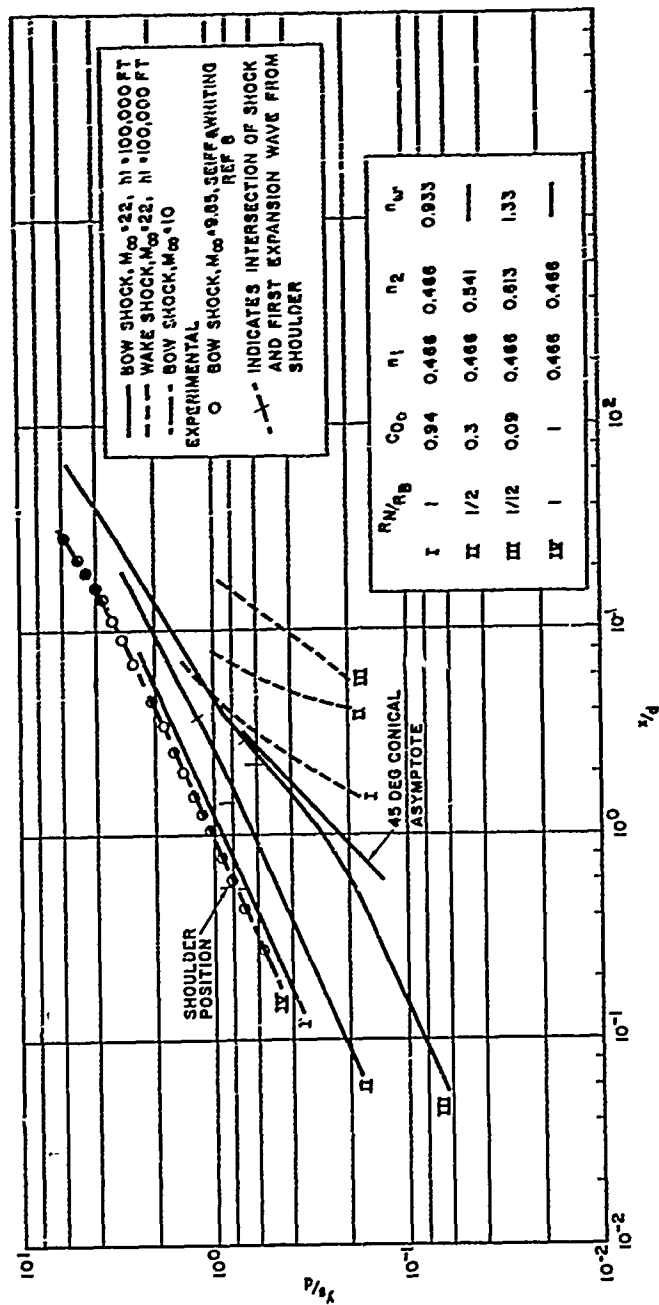


Figure 5. Computed and Experimental Shock Shapes for Various Sphere-Cones Including Wake Shock

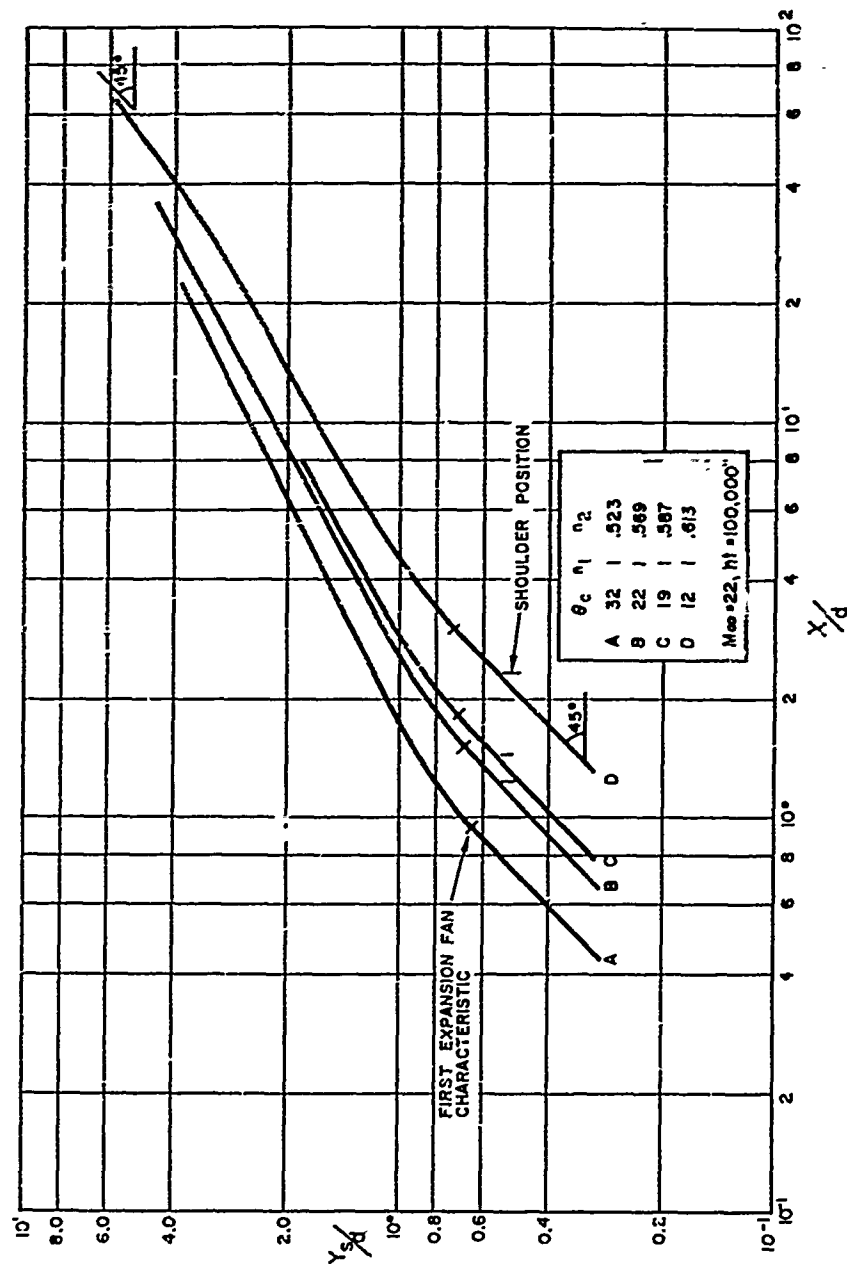


Figure 6. Computed Bow Shock Shapes for Various Cones
($M_\infty = 22$, $h_1 = 100,000$ ft.)

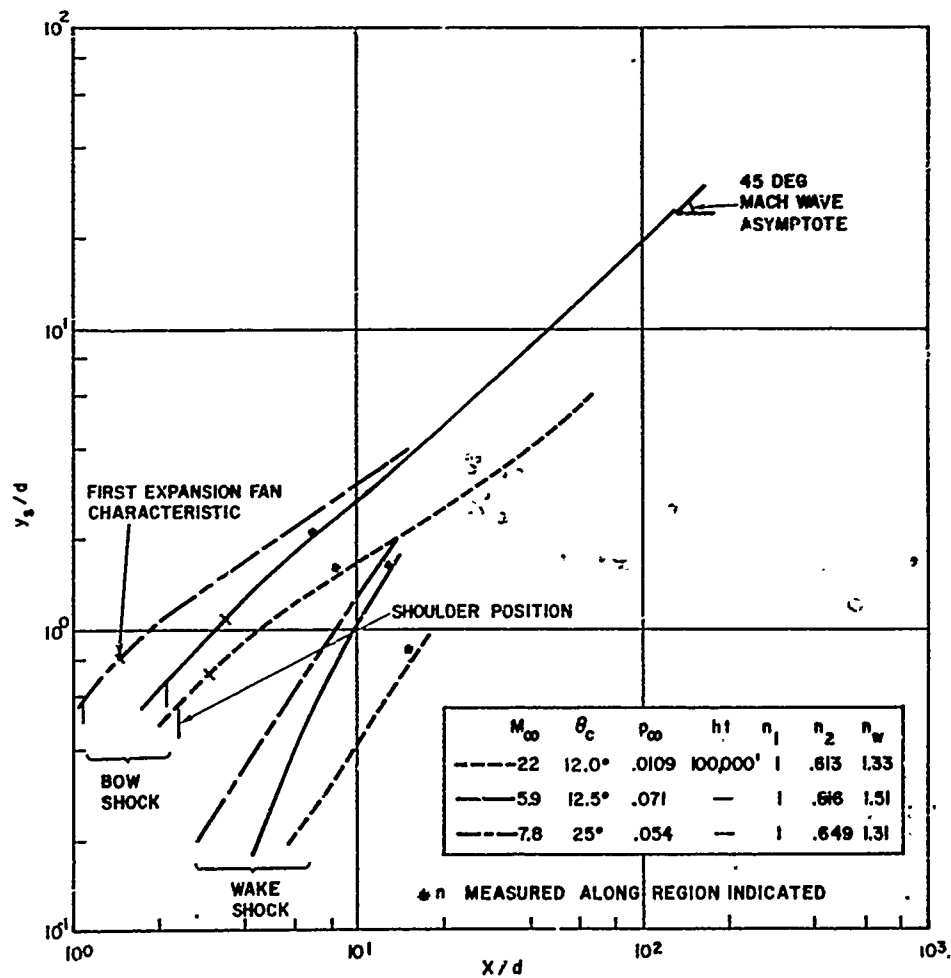


Figure 7. Computed Bow and Wake Shock Shapes for Slender Cones ($M_\infty = 5.9, 7.8$, and 22)

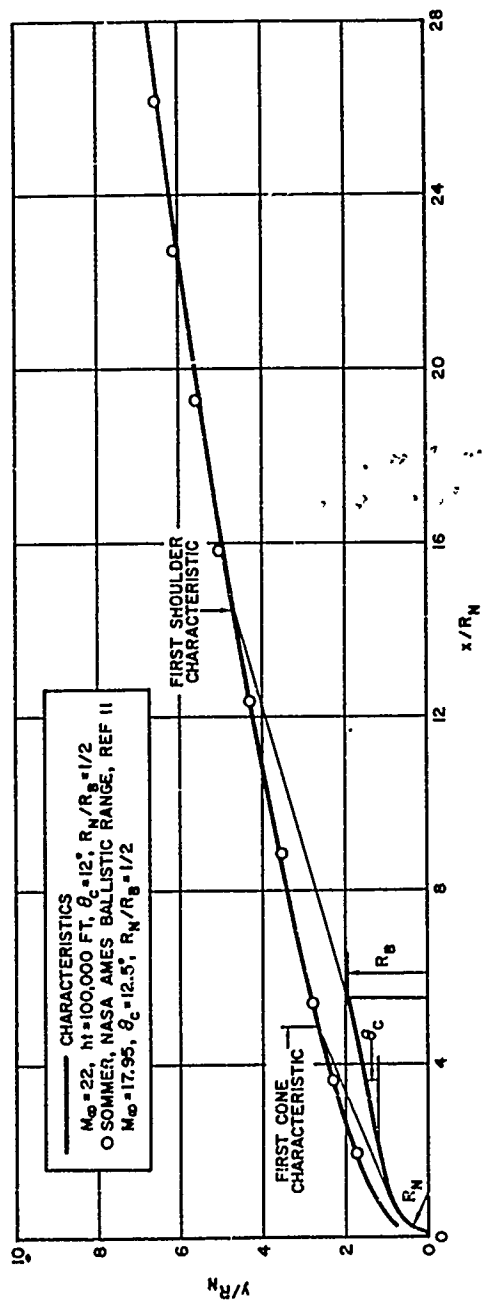


Figure 8. Comparison of Theoretical and Experimental Shock Shape ($R_N/R_B = 1/2$)

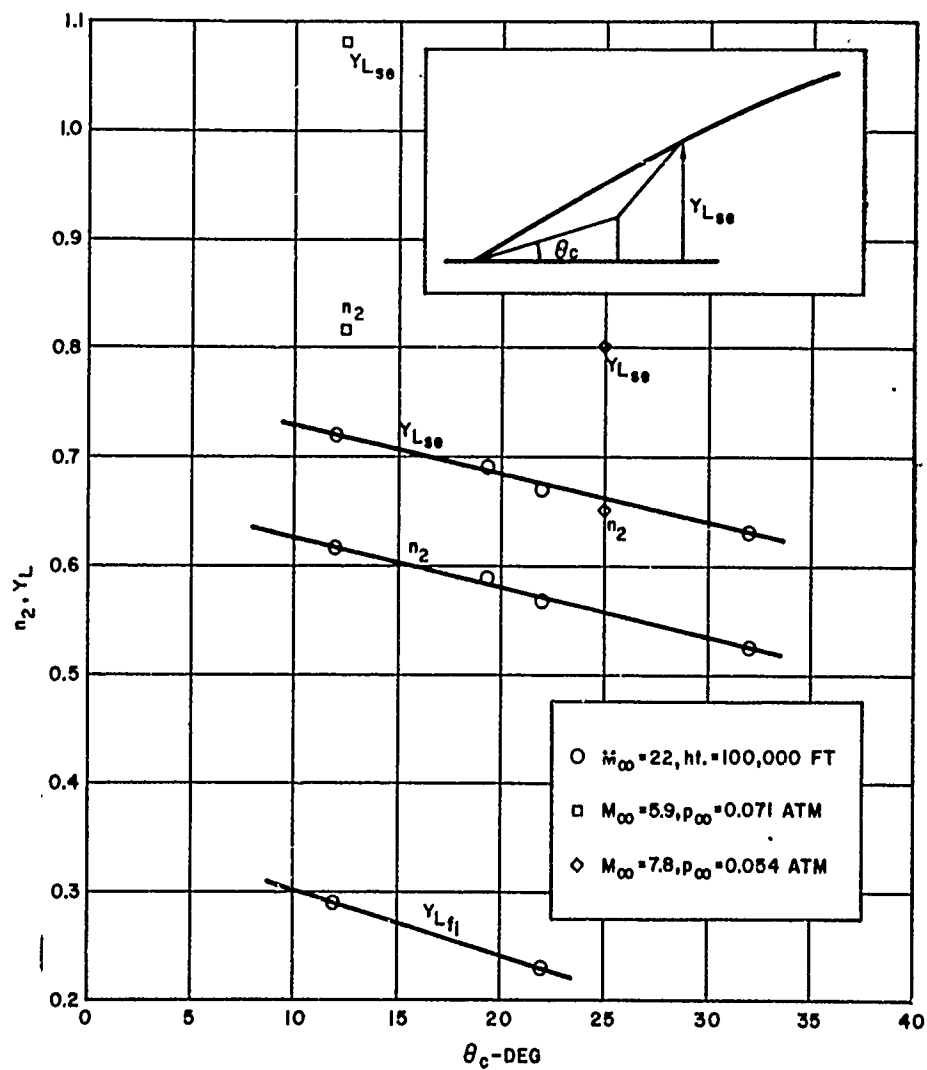


Figure 9. Variation of n_2 , Y_{Lse} and (Y_{Lfi}) vs. Cone Angle

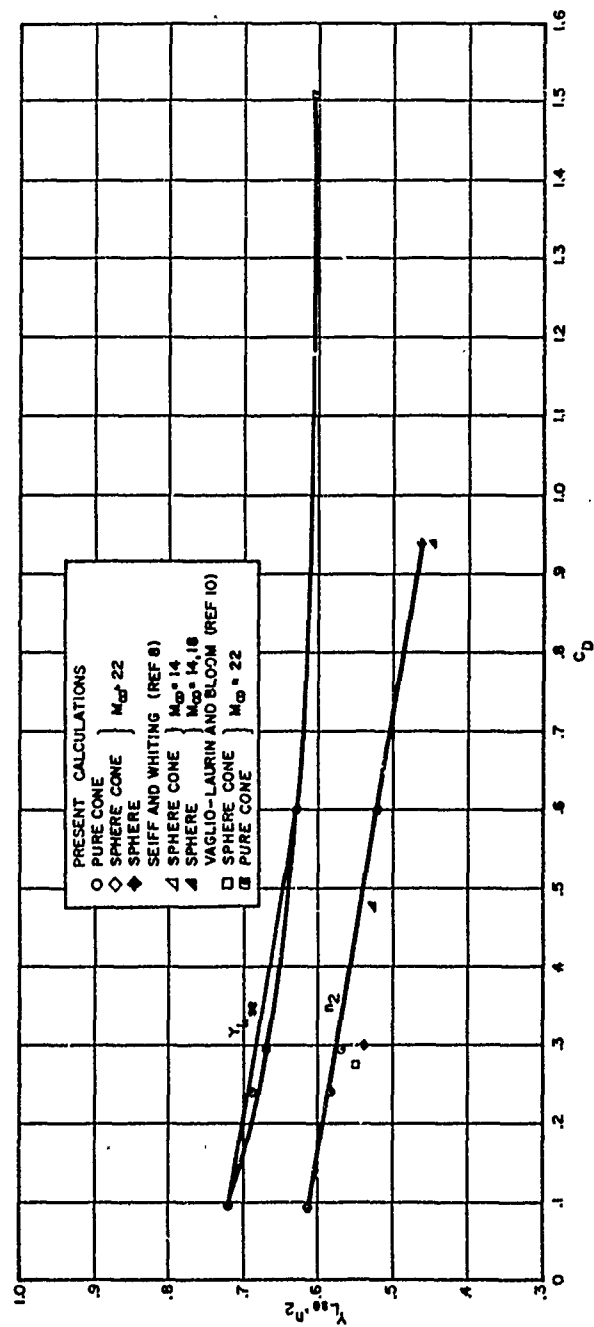


Figure 10. Variation of n_2 and Y_L vs. Drag Coefficient

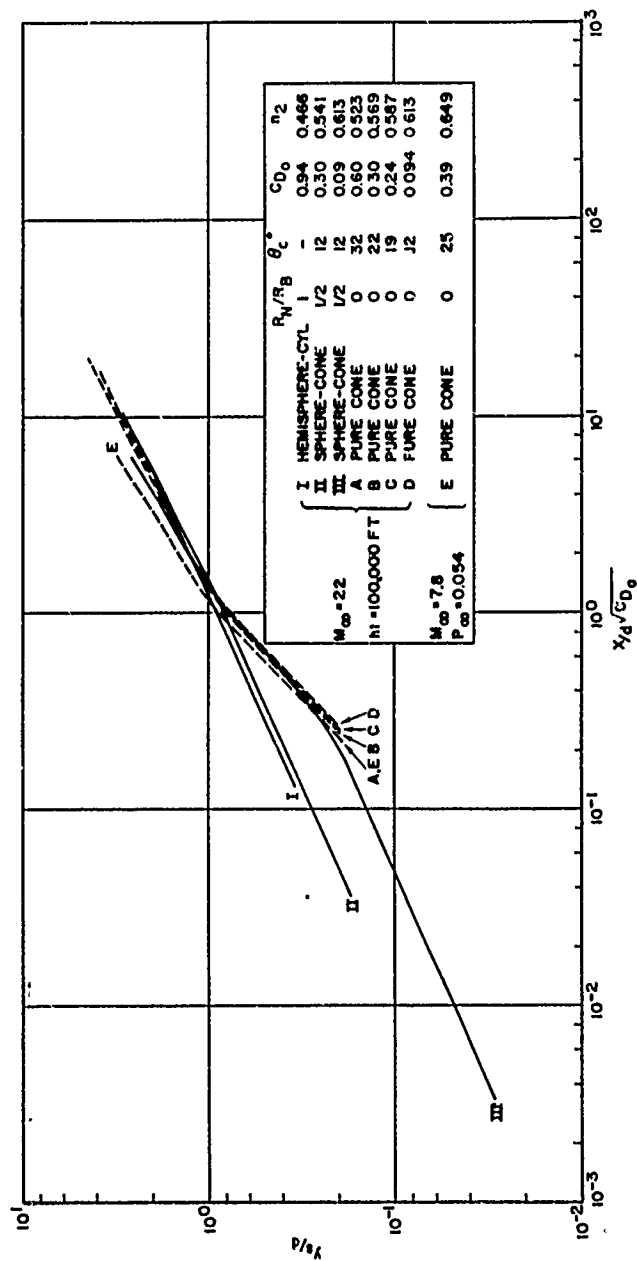


Figure 11. Correlated Bow Shock Shapes for Various Sphere-Cone Combinations

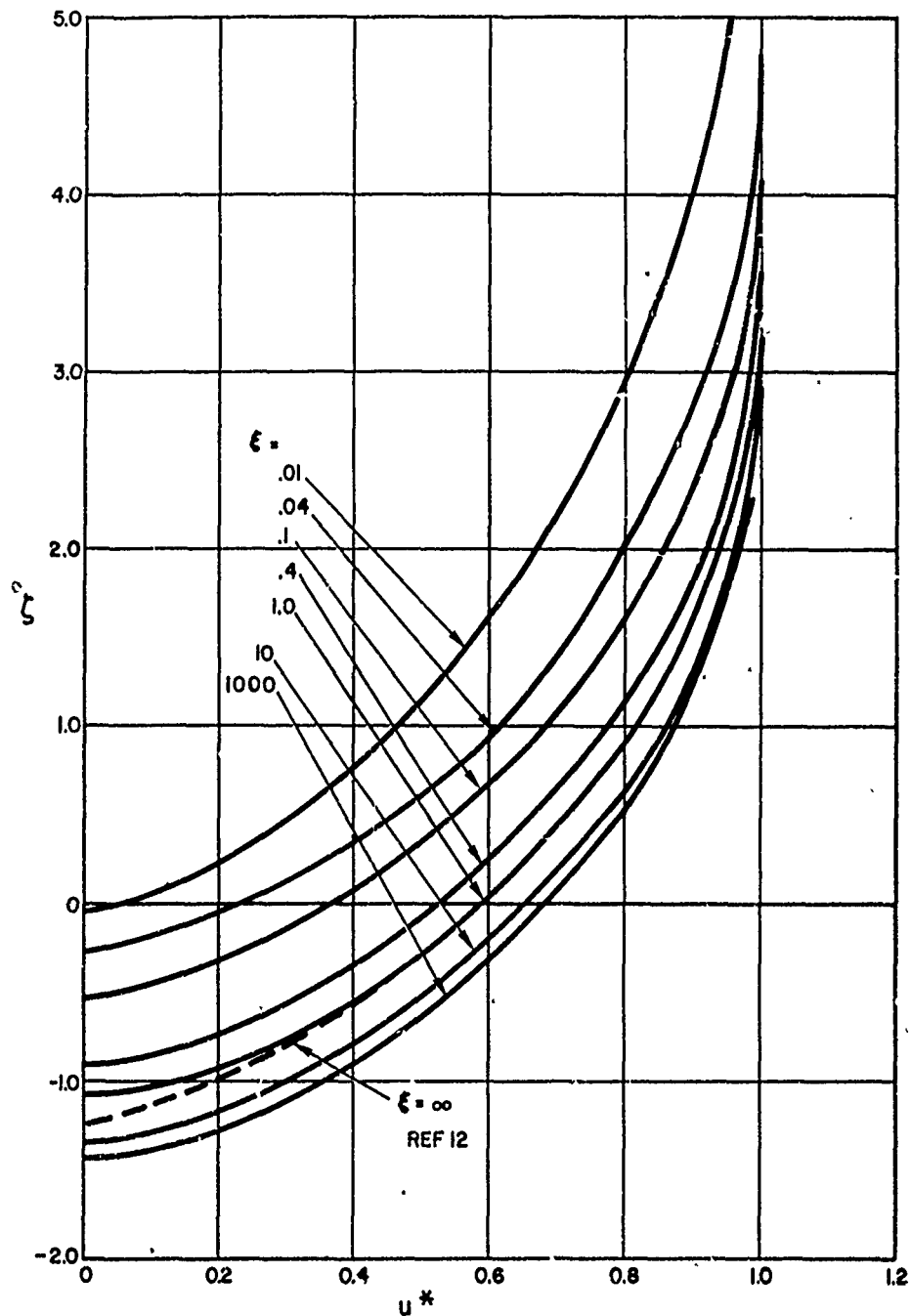


Figure 12. Mixing Layer Velocity as a Function of Mass Flow Parameter for Different Lengths of Separated Mixing Layer

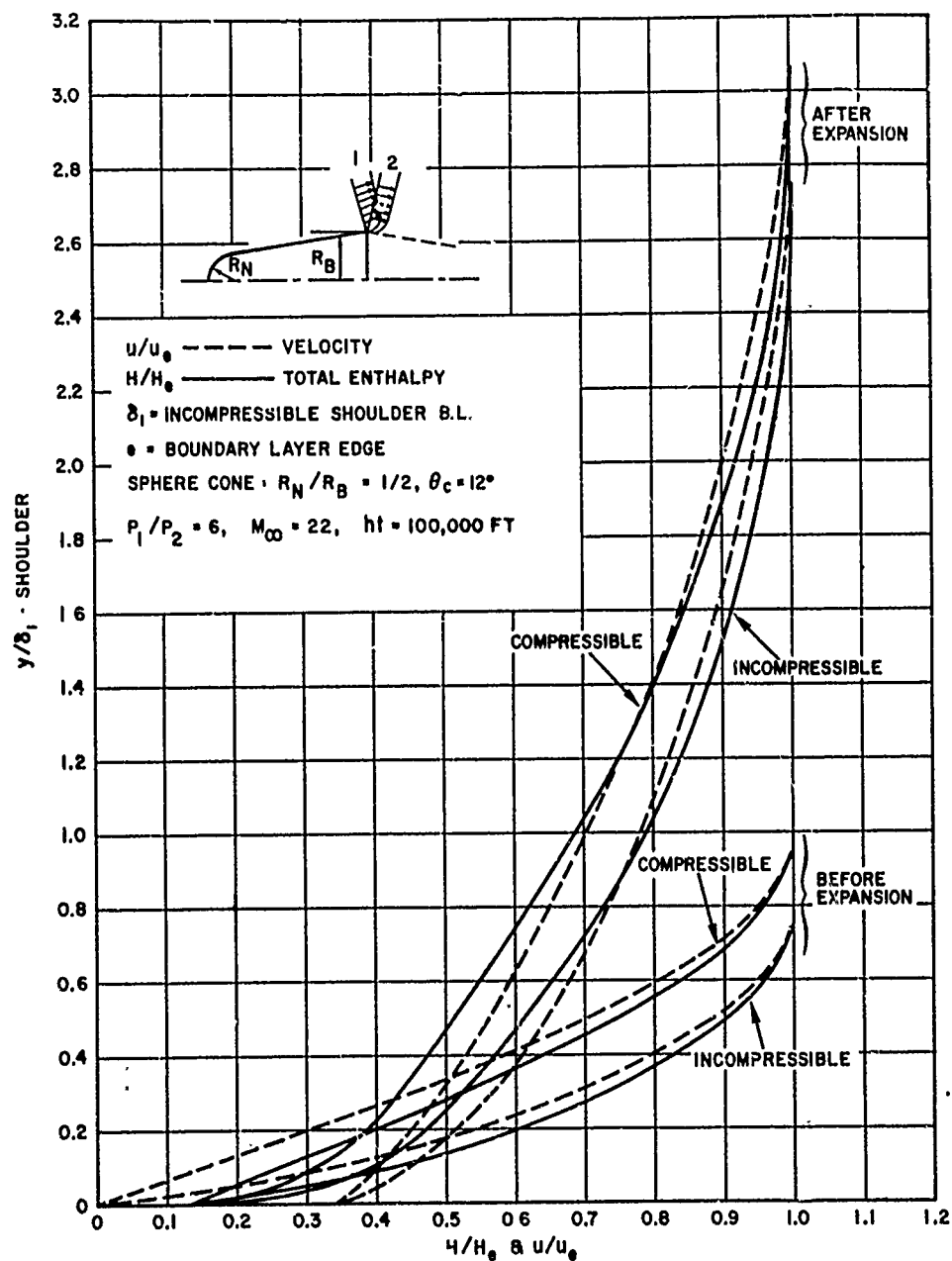


Figure 13. Incompressible and Compressible Boundary Layer Profiles Before and After Base Region Expansion

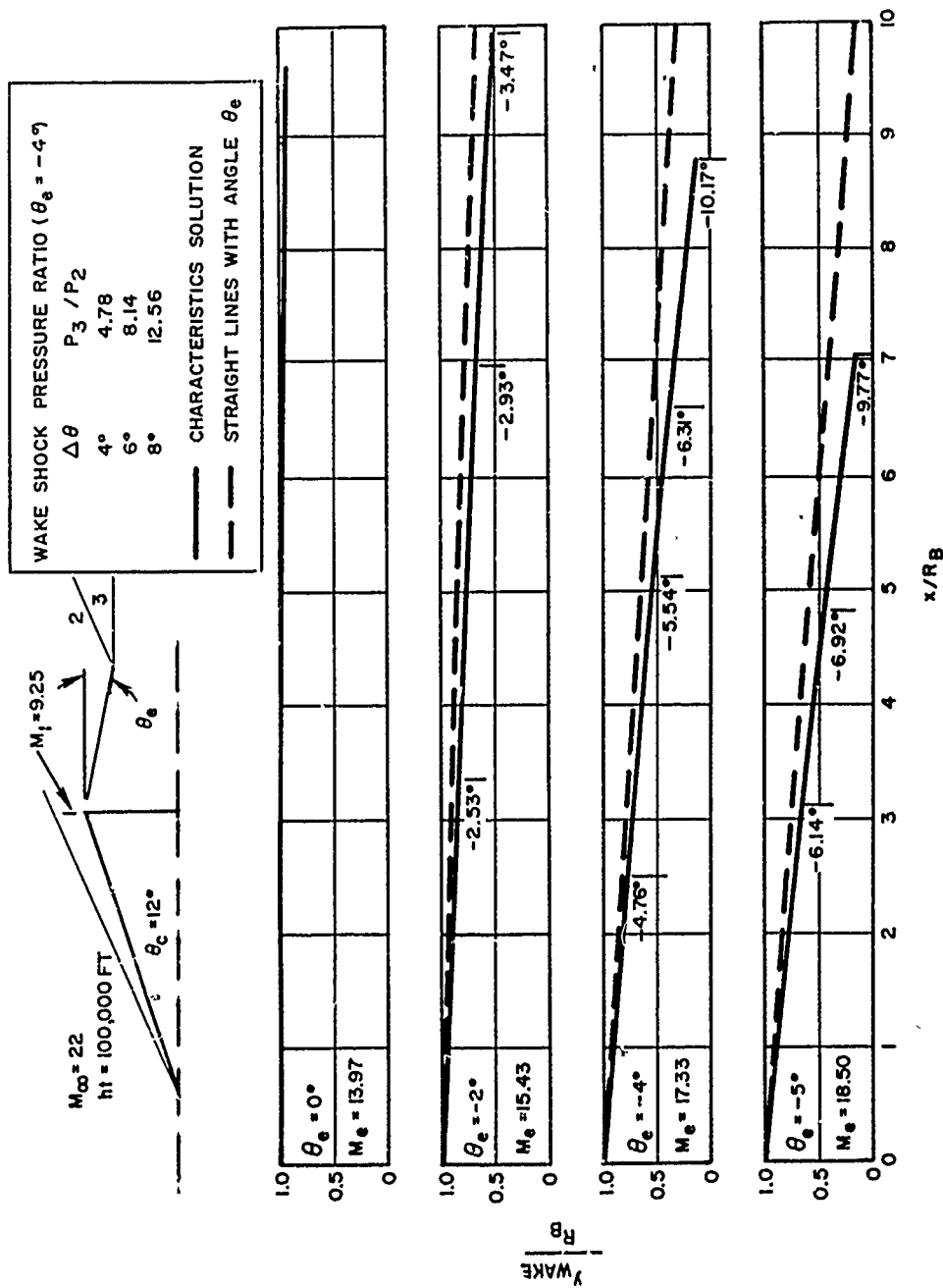


Figure 14. Axi-Symmetric Effect on Base Region Free Streamline
($M_\infty = 22$, $h = 100,000 \text{ ft.}$, $\theta_c = 12^\circ$)

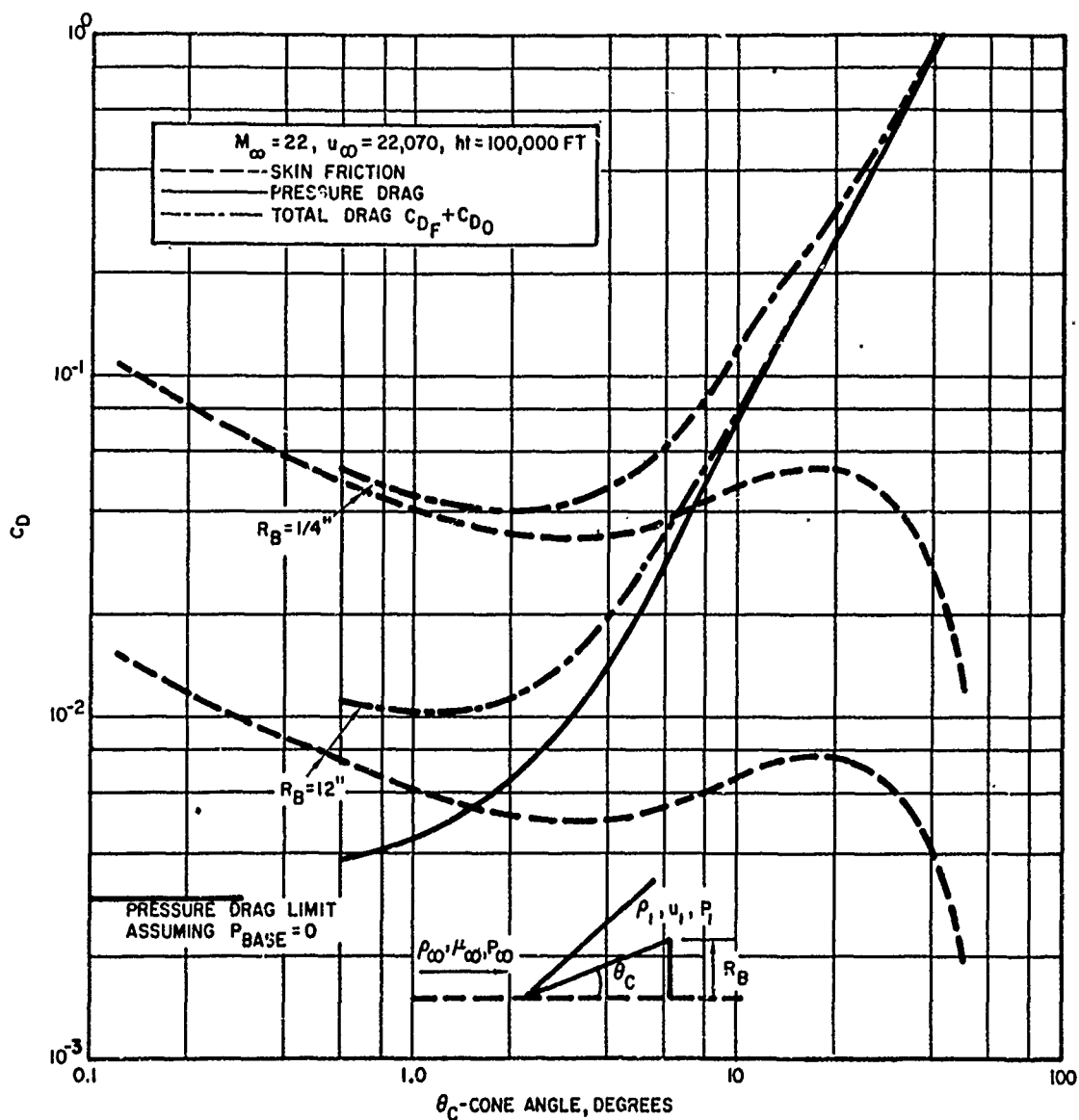
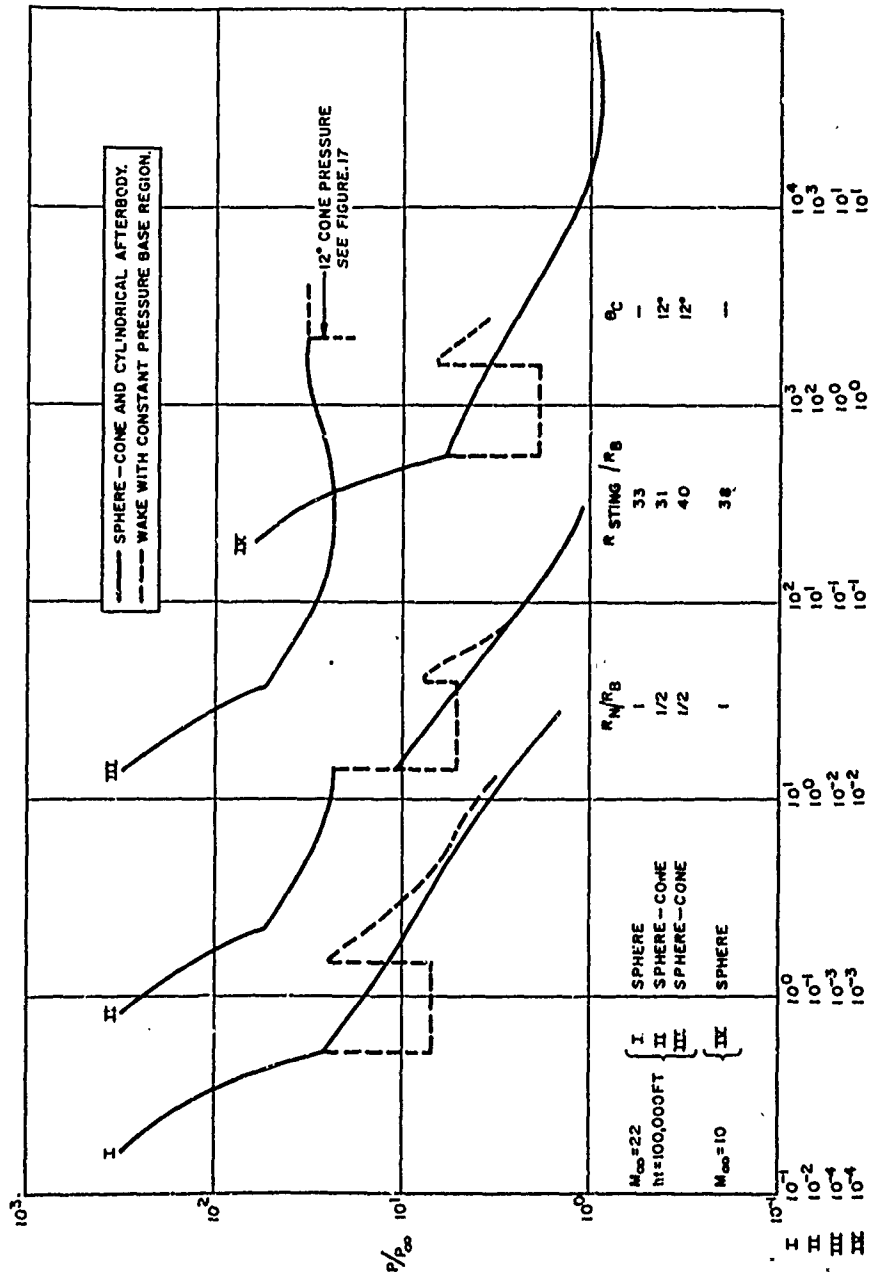


Figure 15. Drag Contributions Due to Pressure and Skin Friction for a Cone ($M_{\infty} = 22, ht = 100,000 \text{ ft.}$)



x/d

Figure 16. Surface and Wake Pressure Distributions for Various Sphere-Cone Combinations

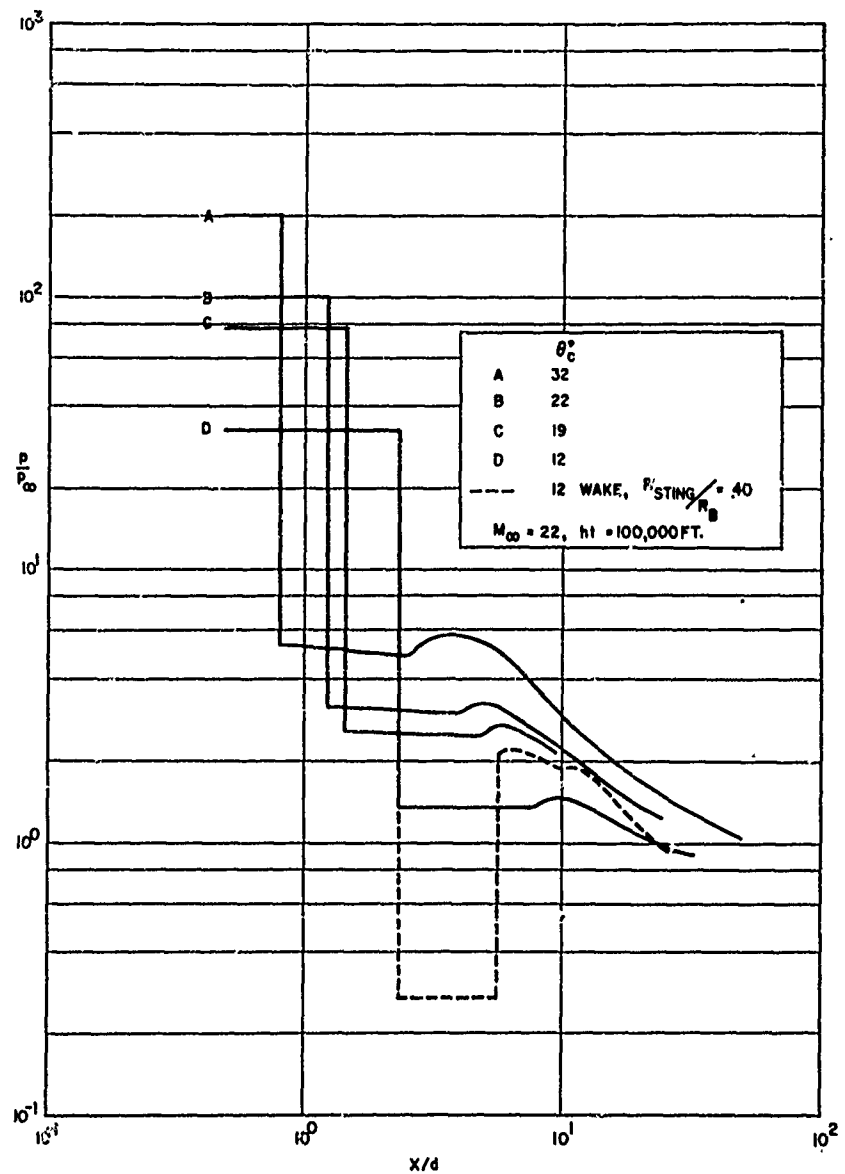


Figure 17. Surface and Wake Pressure Distributions for Various Cones ($M_{\infty} = 22, h_t = 100,000 \text{ ft.}$)

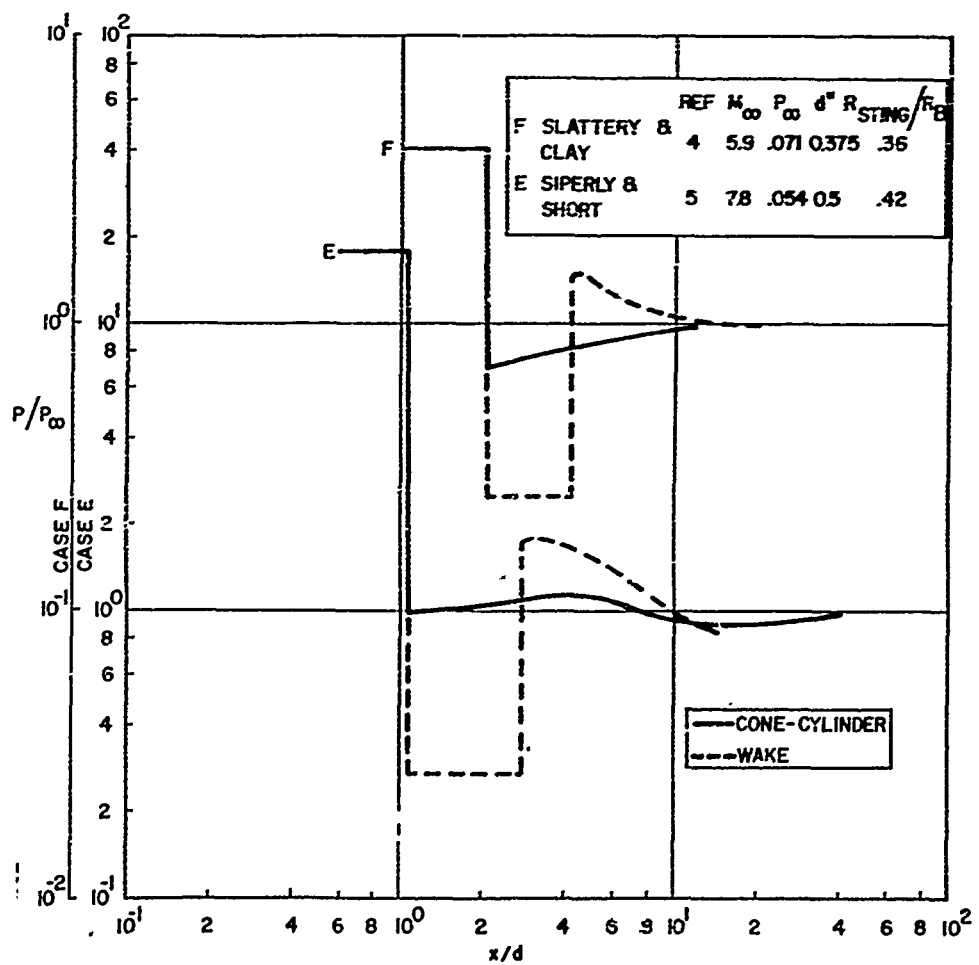


Figure 18. Surface and Wake Pressure Distribution for Ballistic Range Data

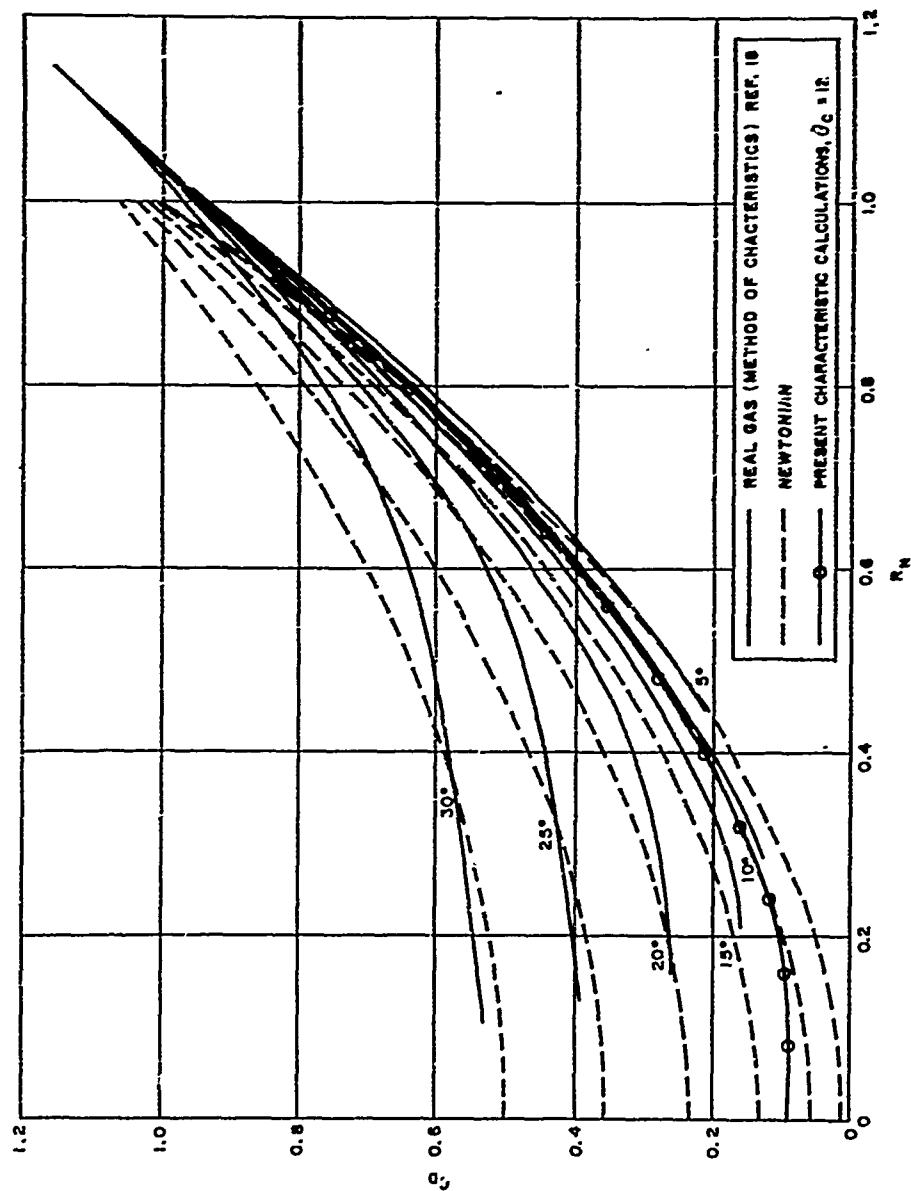


Figure 19. Drag Coefficient for Sphere-Cones (Hypersonic)

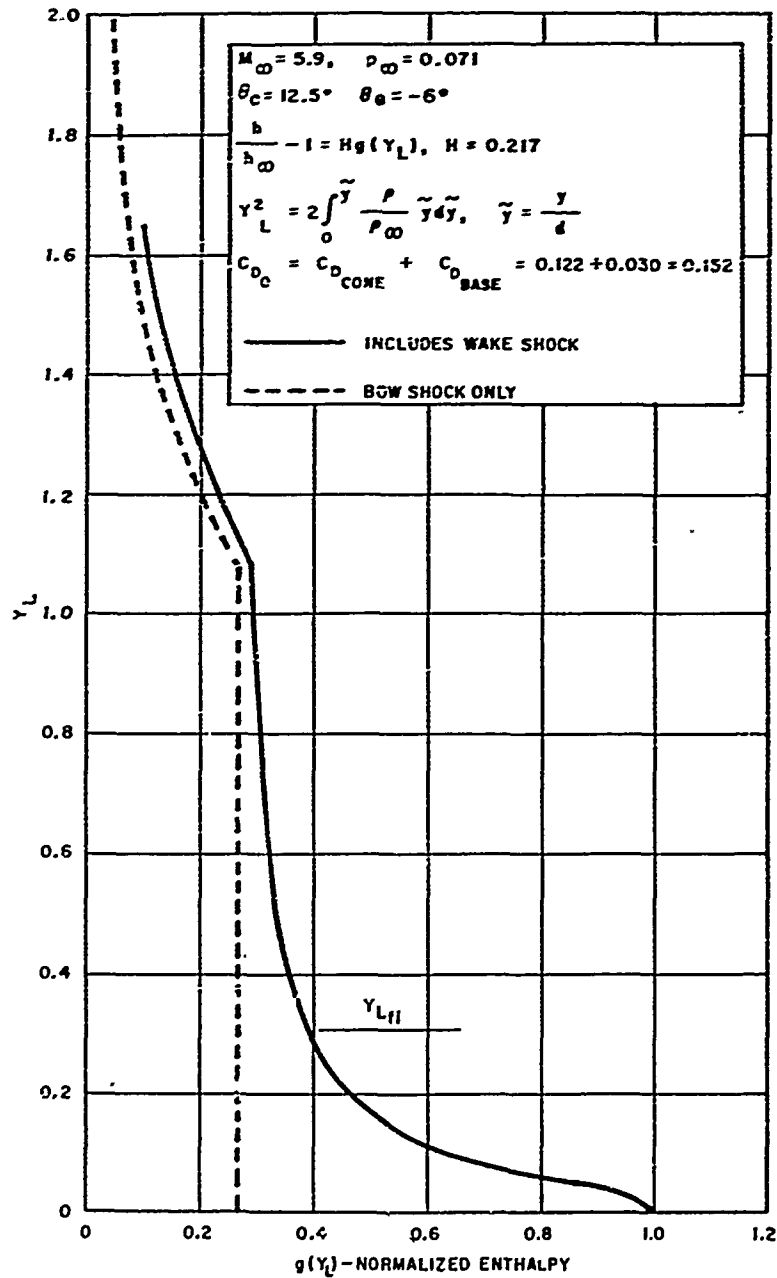


Figure 20. Effect of Wake Shock on Enthalpy Distribution for Conical Body ($M_\infty = 5.9, p_\infty = .071$)

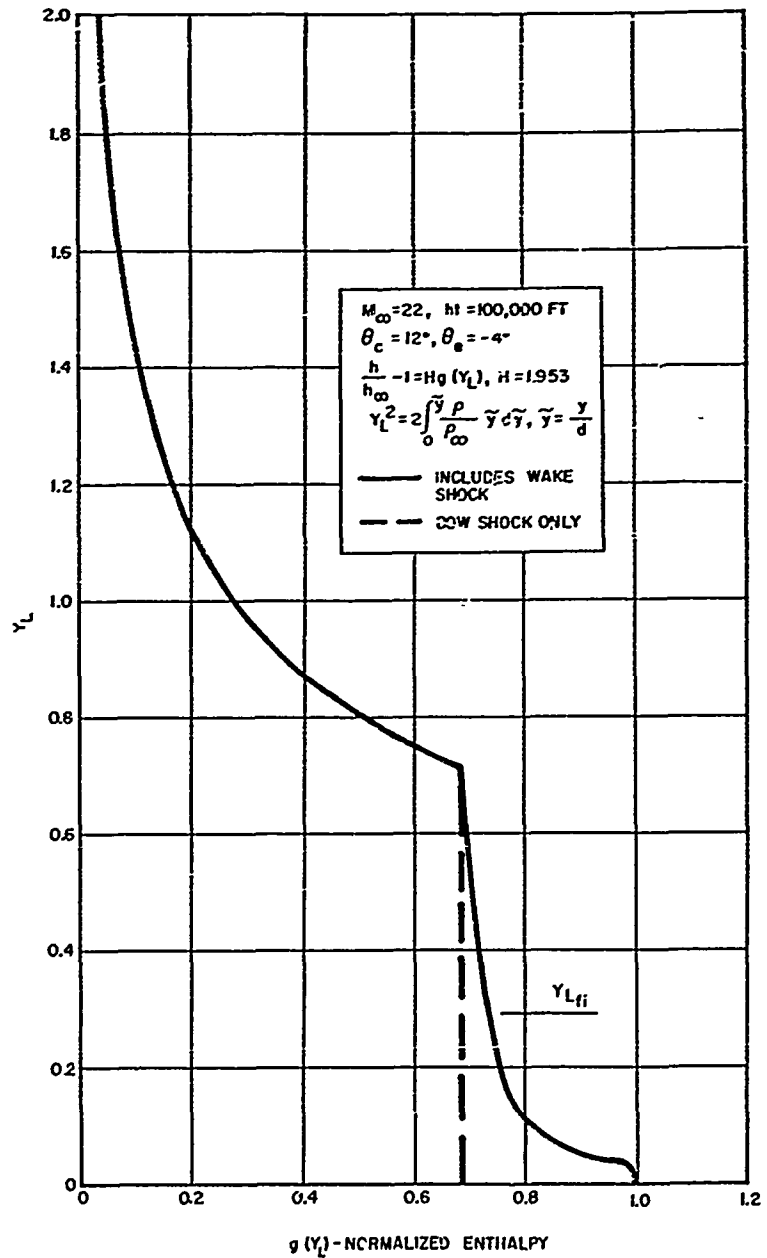


Figure 21. Effect of Wake Shock on Enthalpy Distribution for Conical Body ($M_\infty = 22$, $h_t = 100,000$ ft.)

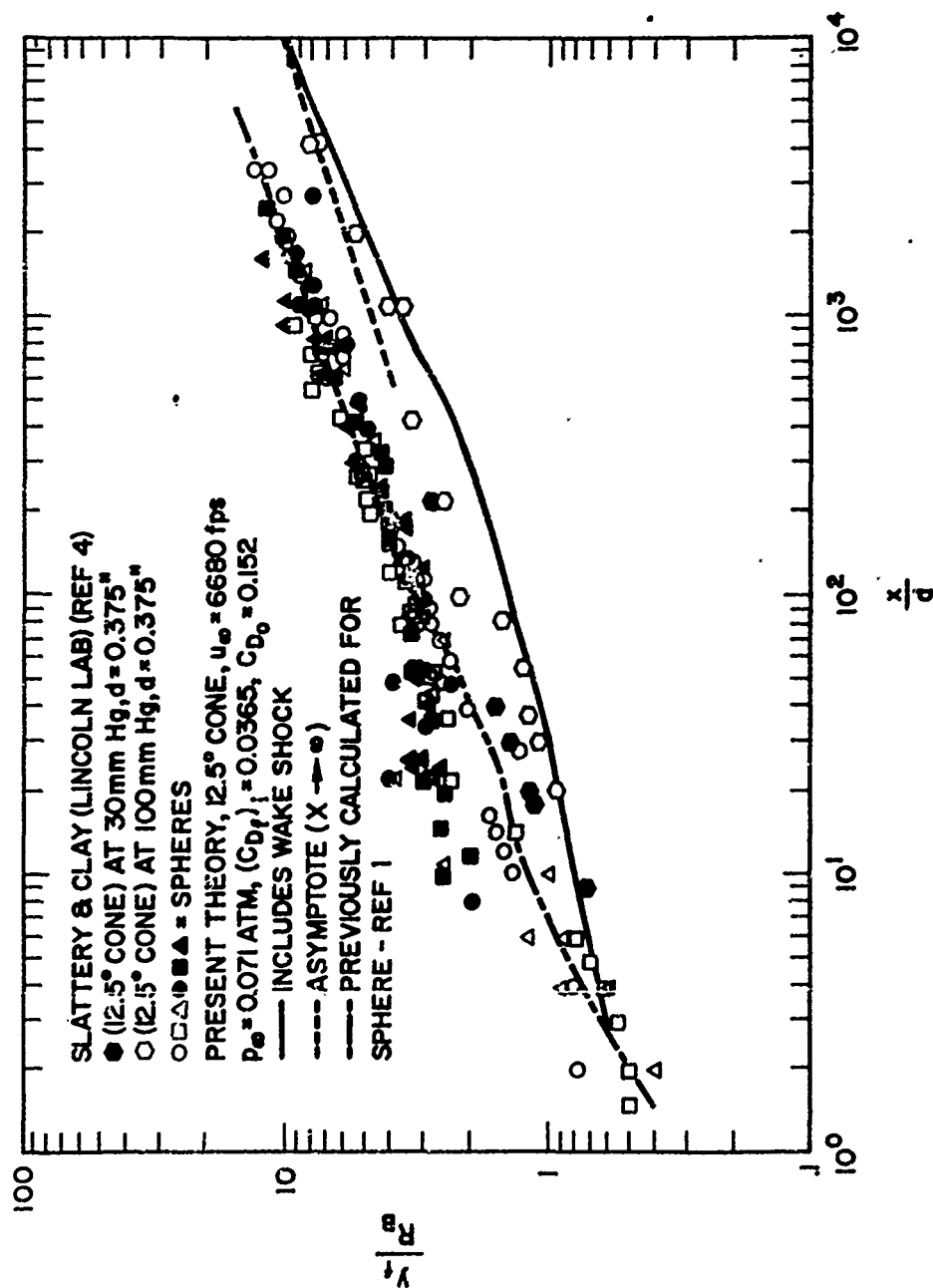


Figure 23. Comparison of Theory and Experiment on Turbulent Wake Width ($M_\infty = 5.9$, $\theta_c = 12.5^\circ$)

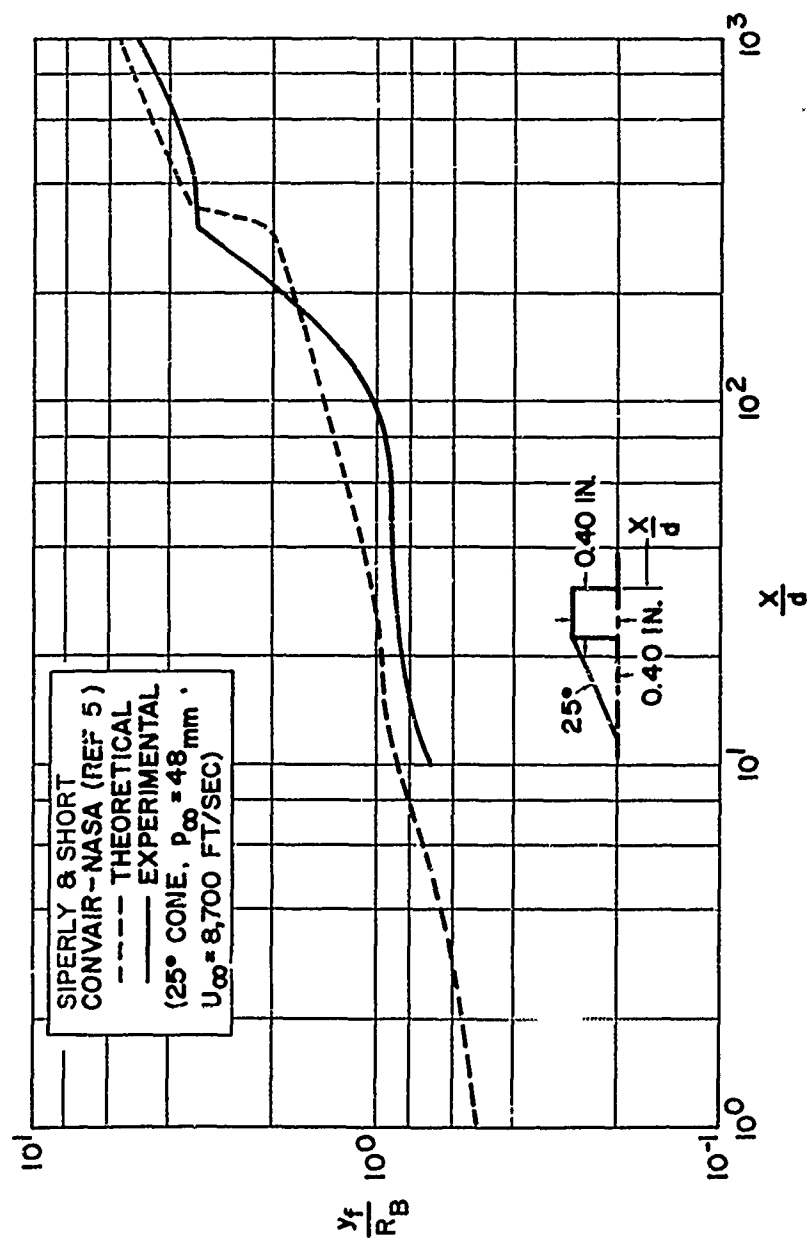


Figure 24. Comparison of Theory and Experiment on Turbulent
 Wake Width ($M_{\infty} = 7.8$, $\theta_c = 25^\circ$)

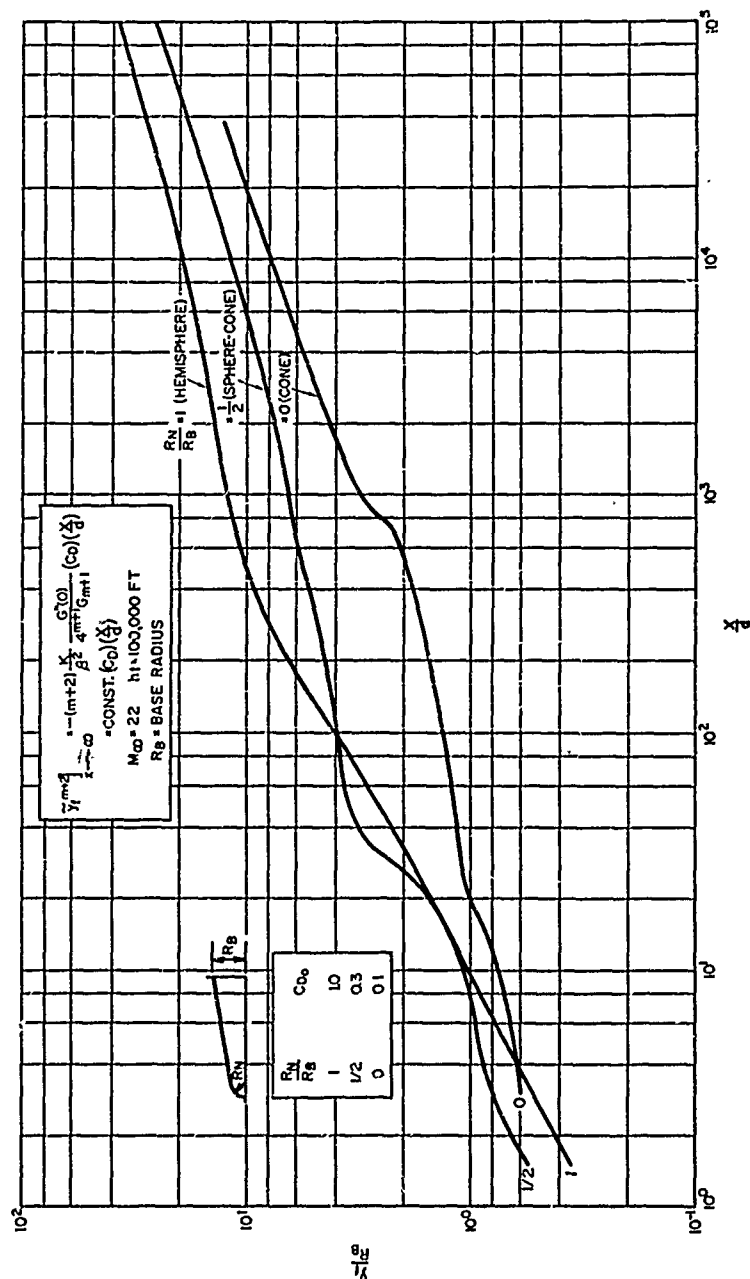


Figure 25. Comparison of Turbulent Wake Width for Different Nose Bluntness ($M_\infty = 22$, $h = 100,000$ ft.)

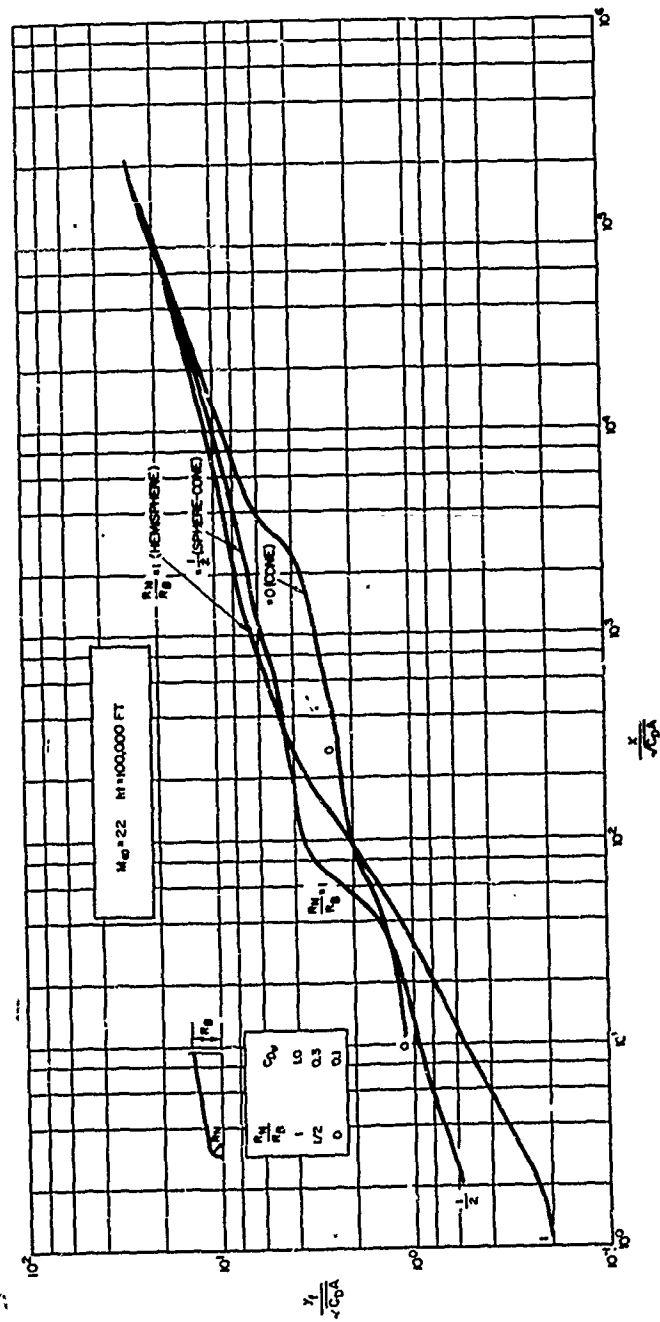


Figure 26. Effect of Nose Bluntness on Growth of Turbulent Wake, "Reduced" Coordinates ($M_\infty = 22$, $h = 100,000$ ft.)

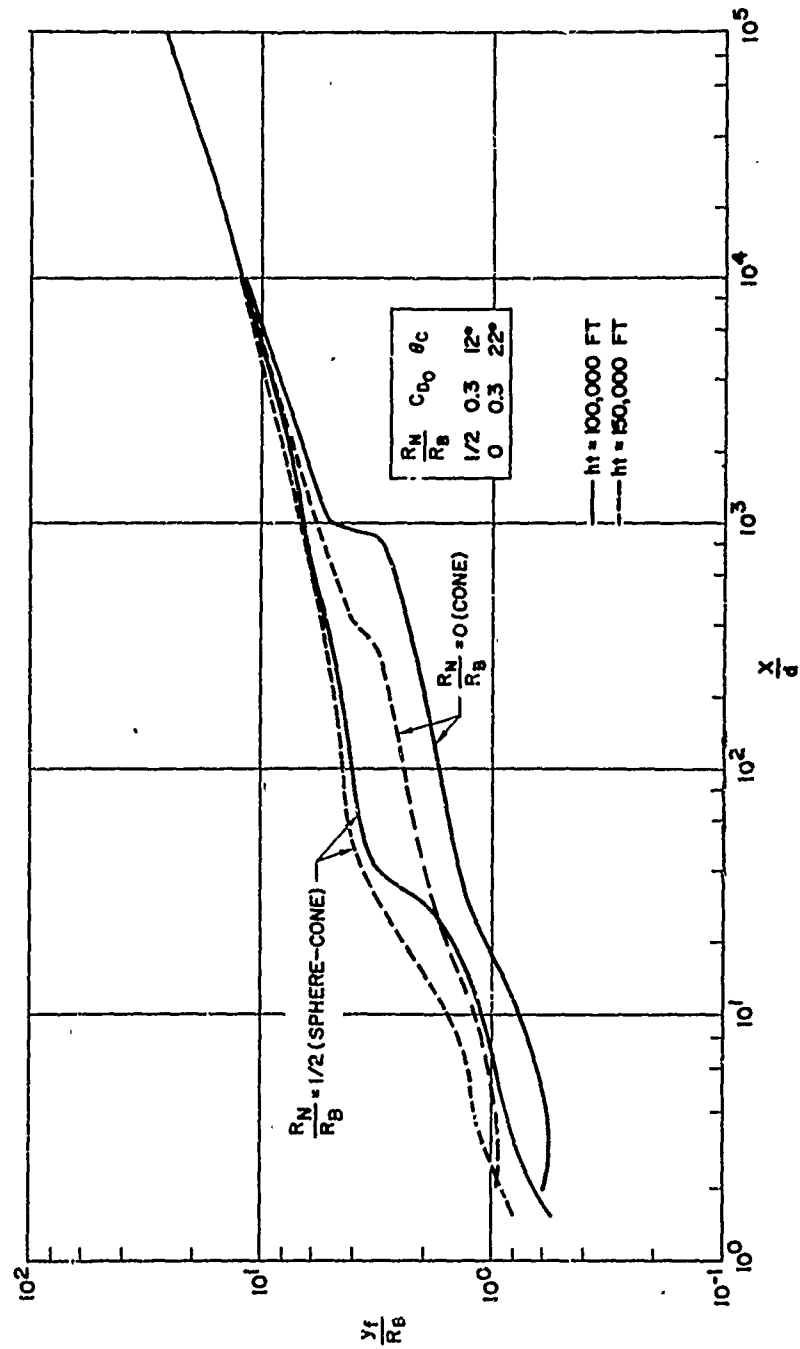


Figure 27. Growth of Turbulent Wake for a Blunt Nosed and a Sharp-Nosed Body With the Same C_{DA}

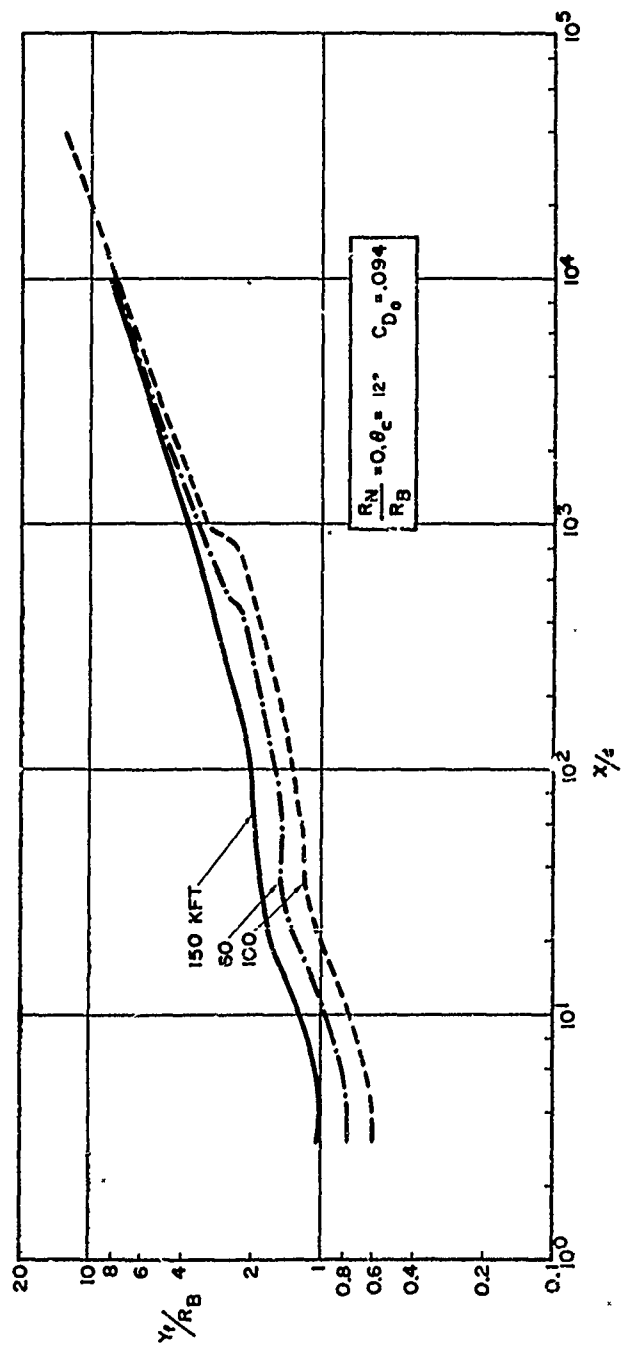


Figure 28. Growth of Turbulent Wake for a 12° Cone at Various Altitudes ($M_\infty = 22$)

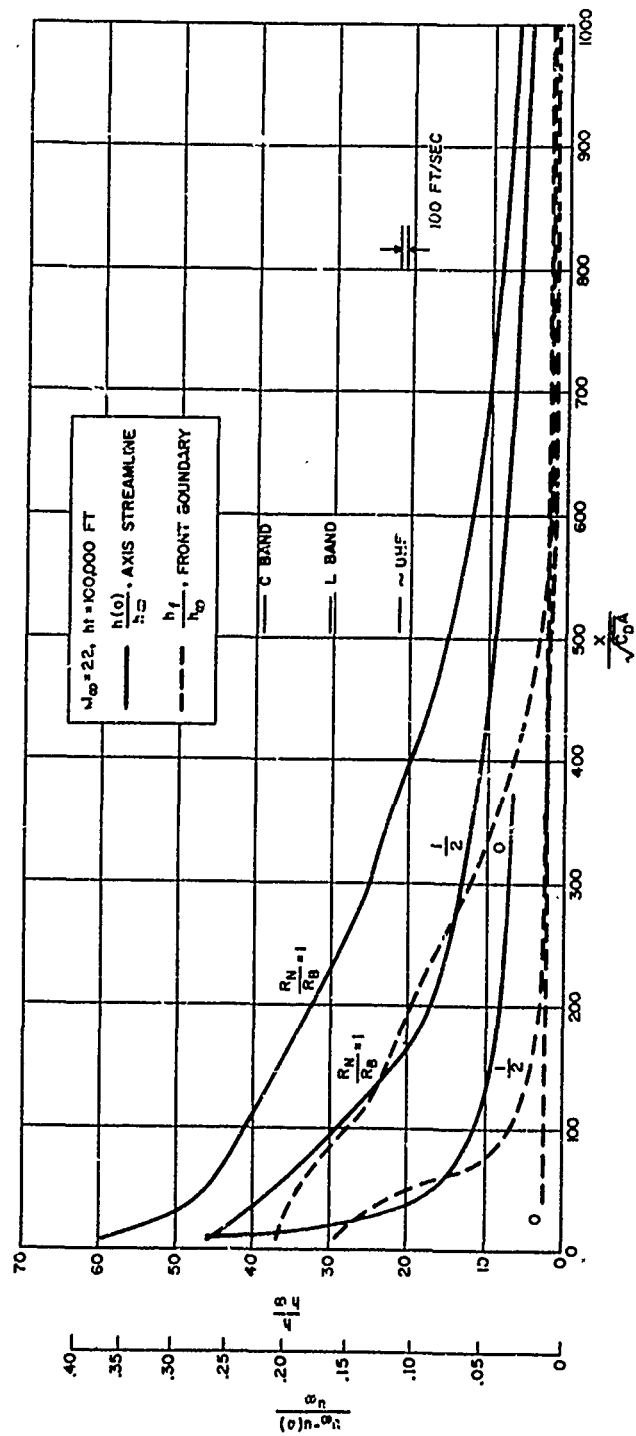


Figure 29. Equilibrium Enthalpy and Velocity Distributions Along Wake Axis and Turbulent Front; ($M_0 = 22$, $N = 100,000$ ft.)

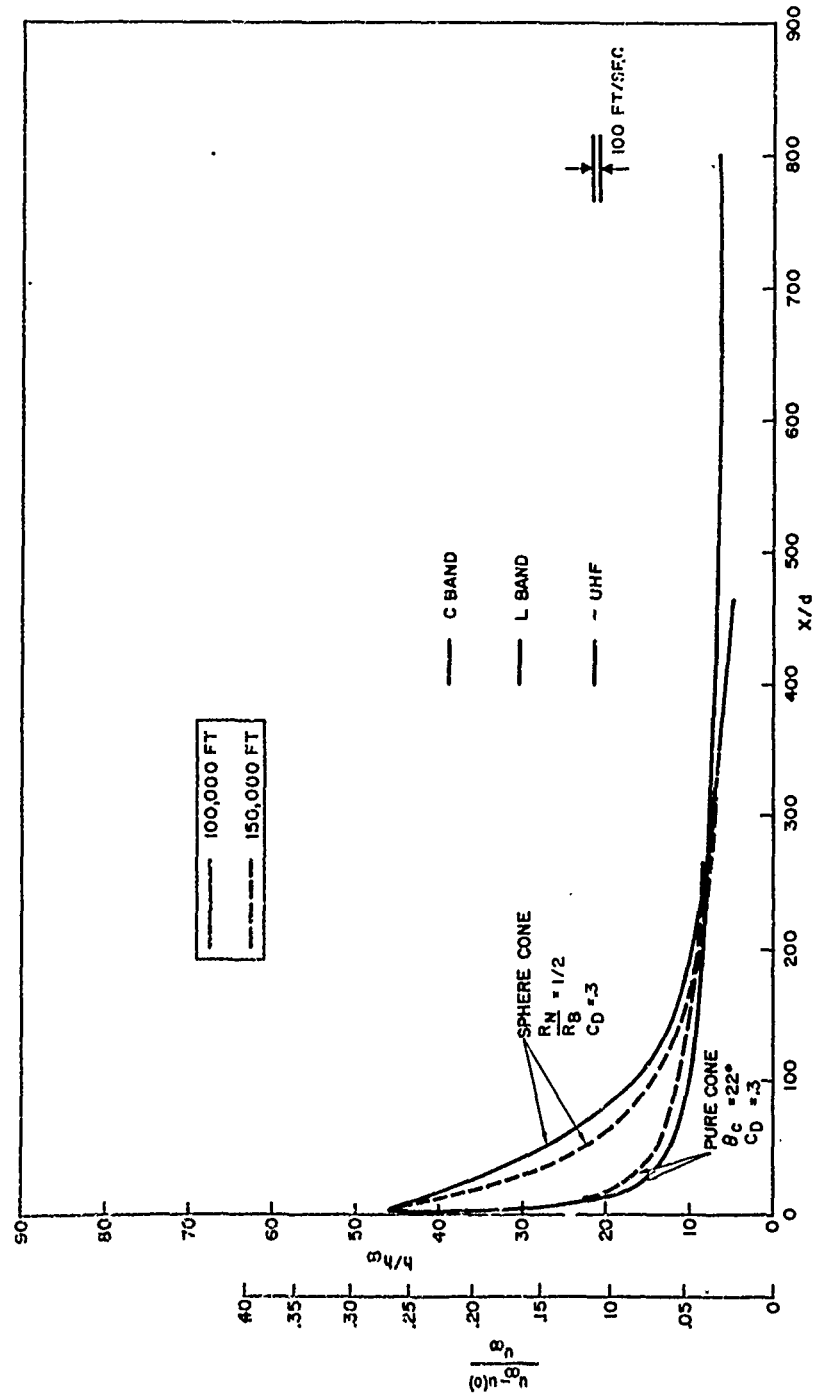


Figure 30. Equilibrium Enthalpy and Velocity Distributions Along Wake Axis for a Blunt Nosed and a Sharp Nosed Body with the Same $C_D A$ ($M_\infty = 22$, $h_t = 100,000$ and $150,000$ ft.)

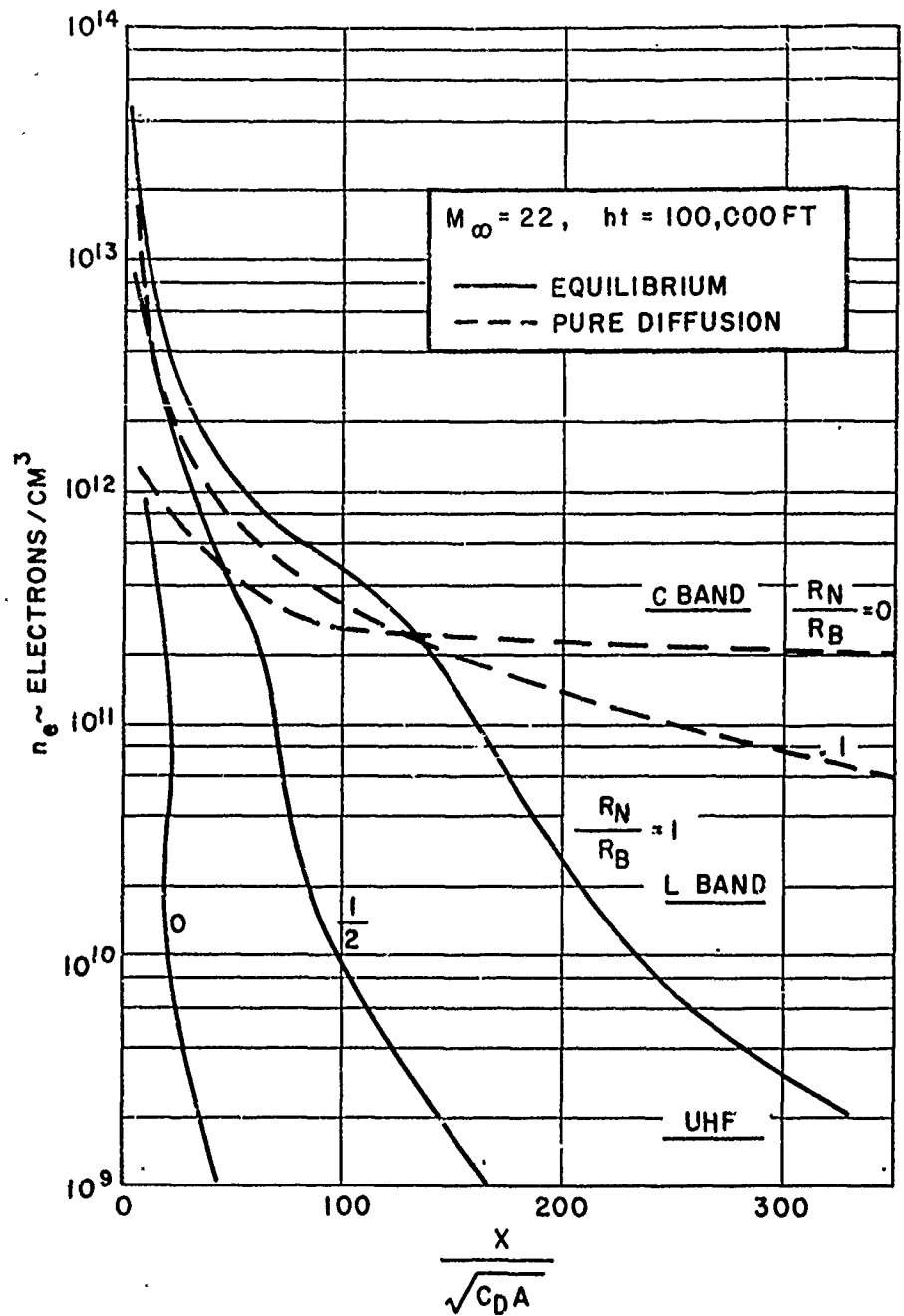


Figure 31. Effect of Nose Bluntness on Electron Density Along Wake Axis
 ($M_{\infty} = 22, h_t = 100,000 \text{ ft.}$)

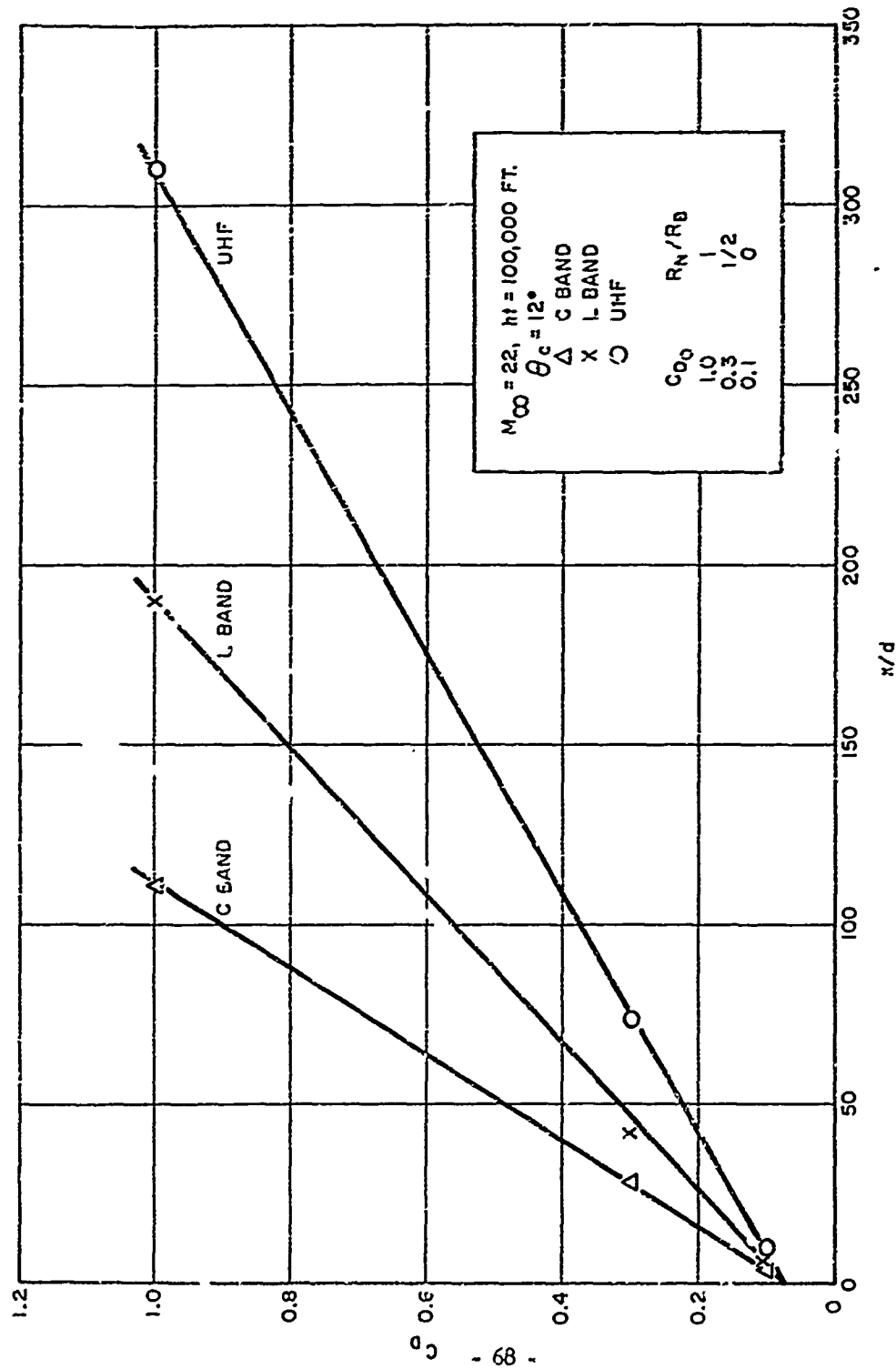


Figure 32. Wake Length as a Function of Drag Coefficient
($M_{\infty} = 22$, $h = 100,000$ ft., $\theta_c = 12^\circ$)

Space Technology Laboratories, Inc., One Space
Park, Redondo Beach, California
REPORT OF NOISE HUNTRESS ON THE TURBULENT HYPERSONIC
WAKE, by Leslie A. Brown and Lester Lees
October, 1962. 68 p. Incl. illus.
6130-6239-N0000 RSD-TDR-62-34
(Contract AF 64(624)-1) Unclassified Report

The effect of body geometry on the equilibrium turbulent hypersonic wake is examined by computing the wake behind several bodies with different cone and sphere-cone nose shapes. Typical re-entry trajectories at several different altitudes are used for the free stream conditions. Also, theoretical predictions for the wake growth behind cones are compared with available ballistic range measurements.

In order to determine the initial conditions for the subsequent wake behavior the bow shock shape, the viscous base and neck regions, and the inviscid wake shock are examined. The results for the initial wake properties indicate that the inviscid flow is much colder by making the body sufficiently slender,

(over)

Unclassified

Unclassified

Space Technology Laboratories, Inc., One Space
Park, Redondo Beach, California
REPORT OF NOISE HUNTRESS ON THE TURBULENT HYPERSONIC
WAKE, by Leslie A. Brown and Lester Lees
October, 1962. 68 p. Incl. illus.
6130-6239-N0000 RSD-TDR-62-34
(Contract AF 64(624)-1) Unclassified Report

The effect of body geometry on the equilibrium turbulent hypersonic wake is examined by computing the wake behind several bodies with different cone and sphere-cone nose shapes. Typical re-entry trajectories at several different altitudes are used for the free stream conditions. Also, theoretical predictions for the wake growth behind cones are compared with available ballistic range measurements.

In order to determine the initial conditions for the subsequent wake behavior the bow shock shape, the viscous base and neck regions, and the inviscid wake shock are examined. The results for the initial wake properties indicate that the inviscid flow is much colder by making the body sufficiently slender,

(over)

Unclassified

Unclassified

Space Technology Laboratories, Inc., One Space
Park, Redondo Beach, California
REPORT OF NOISE HUNTRESS ON THE TURBULENT HYPERSONIC
WAKE, by Leslie A. Brown and Lester Lees
October, 1962. 68 p. Incl. illus.
6130-6239-N0000 RSD-TDR-62-34
(Contract AF 64(624)-1) Unclassified Report

The effect of body geometry on the equilibrium turbulent hypersonic wake is examined by computing the wake behind several bodies with different cone and sphere-cone nose shapes. Typical re-entry trajectories at several different altitudes are used for the free stream conditions. Also, theoretical predictions for the wake growth behind cones are compared with available ballistic range measurements.

In order to determine the initial conditions for the subsequent wake behavior the bow shock shape, the viscous base and neck regions, and the inviscid wake shock are examined. The results for the initial wake properties indicate that the inviscid flow is much colder by making the body sufficiently slender,

(over)

Unclassified

Space Technology Laboratories, Inc., One Space
Park, Redondo Beach, California
REPORT OF NOISE HUNTRESS ON THE TURBULENT HYPERSONIC
WAKE, by Leslie A. Brown and Lester Lees
October, 1962. 68 p. Incl. illus.
6130-6239-N0000 RSD-TDR-62-34
(Contract AF 64(624)-1) Unclassified Report

The effect of body geometry on the equilibrium turbulent hypersonic wake is examined by computing the wake behind several bodies with different cone and sphere-cone nose shapes. Typical re-entry trajectories at several different altitudes are used for the free stream conditions. Also, theoretical predictions for the wake growth behind cones are compared with available ballistic range measurements.

In order to determine the initial conditions for the subsequent wake behavior the bow shock shape, the viscous base and neck regions, and the inviscid wake shock are examined. The results for the initial wake properties indicate that the inviscid flow is much colder by making the body sufficiently slender,

(over)

Unclassified

even though the wake shock now gives a relatively significant contribution to the enthalpy. Also it is found that in determining the initial viscous core properties the Reynolds number is much more important than the shape of the body.

From the downstream wake histories the results indicate that initially the slender body wake grows slower and cools much faster than the blunt body wake. Eventually, sufficiently far downstream the wakes of all bodies should be a unique function of $C_D A$. However, until the asymptotic downstream condition occurs, it is found that even two bodies with the same drag coefficient but different shapes can have completely different wake growth and enthalpy histories. Further, the degree of this difference depends considerably on the altitude (Reynolds number). Since equilibrium electron histories follow the enthalpy, a slender cone can have a very short radar wake compared to a blunt body. On the other hand, because of the initially slower wake growth for the cone an even longer time then for the blunt body can be required for the radial diffusion of any non-recombining foreign substance (e.g., ablation material) deposited in the wake.

even though the wake shock now gives a relatively significant contribution to the enthalpy. Also it is found that in determining the initial viscous core properties the Reynolds number is much more important than the shape of the body.

From the downstream wake histories the results indicate that initially the slender body wake grows slower and cools much faster than the blunt body wake. Eventually, sufficiently far downstream the wakes of all bodies should be a unique function of $C_D A$. However, until the asymptotic downstream condition occurs, it is found that even two bodies with the same drag coefficient but different shapes can have completely different wake growth and enthalpy histories. Further, the degree of this difference depends considerably on the altitude (Reynolds number). Since equilibrium electron histories follow the enthalpy, a slender cone can have a very short radar wake compared to a blunt body. On the other hand, because of the initially slower wake growth for the cone an even longer time then for the blunt body can be required for the radial diffusion of any non-recombining foreign substance (e.g., ablation material) deposited in the wake.

Unclassified

Unclassified

Unclassified

Unclassified

even though the wake shock now gives a relatively significant contribution to the enthalpy. Also it is found that in determining the initial viscous core properties the Reynolds number is much more important than the shape of the body.

From the downstream wake histories the results indicate that initially the slender body wake grows slower and cools much faster than the blunt body wake. Eventually, sufficiently far downstream the wakes of all bodies should be a unique function of $C_D A$. However, until the asymptotic downstream condition occurs, it is found that even two bodies with the same drag coefficient but different shapes can have completely different wake growth and enthalpy histories. Further, the degree of this difference depends considerably on the altitude (Reynolds number). Since equilibrium electron histories follow the enthalpy, a slender cone can have a very short radar wake compared to a blunt body. On the other hand, because of the initially slower wake growth for the cone an even longer time then for the blunt body can be required for the radial diffusion of any non-recombining foreign substance (e.g., ablation material) deposited in the wake.

even though the wake shock now gives a relatively significant contribution to the enthalpy. Also it is found that in determining the initial viscous core properties the Reynolds number is much more important than the shape of the body.

From the downstream wake histories the results indicate that initially the slender body wake grows slower and cools much faster than the blunt body wake. Eventually, sufficiently far downstream the wakes of all bodies should be a unique function of $C_D A$. However, until the asymptotic downstream condition occurs, it is found that even two bodies with the same drag coefficient but different shapes can have completely different wake growth and enthalpy histories. Further, the degree of this difference depends considerably on the altitude (Reynolds number). Since equilibrium electron histories follow the enthalpy, a slender cone can have a very short radar wake compared to a blunt body. On the other hand, because of the initially slower wake growth for the cone an even longer time then for the blunt body can be required for the radial diffusion of any non-recombining foreign substance (e.g., ablation material) deposited in the wake.

Unclassified

Unclassified

Unclassified

Unclassified